

Ultrafast Momentum-Resolved Probing of Plasmon Thermal Dynamics with Free Electrons

Vahagn Mkhitarian,^{1,*} Eduardo J. C. Dias,^{1,*} Fabrizio Carbone,² and F. Javier García de Abajo^{1,3,†}

¹*ICFO-Institut de Ciències Fotoniques, The Barcelona Institute of Science and Technology, 08860 Castelldefels (Barcelona), Spain*

²*Laboratory for Ultrafast Microscopy and Electron Scattering (LUMES), Institute of Physics, École Polytechnique Fédérale de Lausanne (EPFL), Lausanne CH-1015, Switzerland*

³*ICREA-Institució Catalana de Recerca i Estudis Avançats, Passeig Lluís Companys 23, 08010 Barcelona, Spain*

Current advances in ultrafast electron microscopy make it possible to combine optical pumping of a nanostructure and electron beam probing with subångstrom and femtosecond spatiotemporal resolution. We present a theory predicting that this technique can reveal a rich out-of-equilibrium dynamics of plasmon excitations in graphene and graphite samples. In a disruptive departure from the traditional probing of nanoscale excitations based on the identification of spectral features in the transmitted electrons, we show that measurement of angle-resolved, energy-integrated inelastic electron scattering can trace the temporal evolution of plasmons in these structures and provide momentum-resolved mode identification, thus avoiding the need for highly-monochromatic electron beams and the use of electron spectrometers. This previously unexplored approach to study the ultrafast dynamics of optical excitations can be of interest to understand and manipulate polaritons in 2D semiconductors and other materials exhibiting a strong thermo-optical response.

I. INTRODUCTION

Thermal engineering of plasmons and other forms of polaritons in nanomaterials offers an appealing way of controlling light-matter interactions down to nanometer [1] and femtosecond [2, 3] spatiotemporal scales, opening applications in photonics and optoelectronics, such as all-optical switching [4, 5], light modulation [6–8], ultrafast light emission [9], and photodetection [10]. Traditionally, the study of ultrafast thermal dynamics relies on optical experiments, in which a light pump pulse is used to excite the system and bring it out of equilibrium, followed by a light probe pulse that measures the evolution of the sample response [11–13]. However, this procedure is limited in spatial resolution due to light diffraction when relying on far-field optics, or to a few tens of nanometers when a tip is used to locally amplify the electromagnetic field in ultrafast scanning near-field optical microscopy (SNOM) [2].

Electron energy-loss spectroscopy (EELS) performed in scanning transmission electron microscopes overcomes the optical diffraction limit by using 30 – 300 keV electrons rather than light to map the material response [14–16] with subångstrom spatial precision [17] and increasing spectral resolution that currently enables the study of mid-infrared polaritons [18–22]. When the electron beam is well collimated, momentum-resolved inelastic electron scattering grants us access into the dispersion relations of surface modes in planar films [23–26], while the dispersion of thicker samples can be probed with lower spatial resolution through low-energy ($\sim 50 - 500$ eV) elec-

tron microscopy in reflection mode [27, 28]. Additionally, a combination of high temporal and spatial resolution has been achieved through the development of ultrafast electron microscopy, based on the use of femtosecond light and electron pulses that are simultaneously aimed at the sample with a well-controlled relative delay [29–31]. By scanning the light frequency, this approach additionally brings meV energy resolution in what is known as electron energy-gain spectroscopy (EEGS) [32–34], which has been experimentally demonstrated [35] to challenge the state-of-the-art benchmark of a few meV achieved through tour-de-force advances in electron optics [18]. In the photon-induced near-field electron microscopy (PINEM) technique [31, 36–46], the electron beam is focused with nanoscale spatial precision, while the relative light-electron delay provides femtosecond temporal resolution. PINEM has been used to shoot femtosecond movies from surface plasmons evolving in nanowires [38] and buried interfaces [40], and more recently, also in the characterization of optical dielectric cavities [45, 46]. Although efforts in this context have emphasized light-matter interaction aspects and our ability to modulate the wave function of free-space electrons, the optical-pump/electron-probe (OPEP) approach has strong potential to study nanoscale dynamics with unrivalled spatiotemporal resolution by addressing material properties that range from relatively slow structural [29, 30] and electronic [47] behavior to the intrinsically ultrafast nonlinear optical response [48].

Two-dimensional (2D) materials offer a splendid testbed for OPEP because they generally undergo substantial changes in their electronic structure under optical pumping. We consider in particular highly-doped graphene, which in addition hosts electrically-tunable plasmons [49–56] that possess long lifetime [57, 58], strong spatial confinement [59, 60], and a large nonlinear

*These two authors contributed equally to the work.

†Electronic address: javier.garciadeabajo@nanophotonics.es

response [5, 61–63]. These properties have prompted the exploration of exciting applications that include infrared photodetection [10, 64–67], optical sensing [68–70], and light modulation [3, 5, 62, 71, 72]. Because of its conical electronic band structure, the thermo-optical response is remarkably high in graphene and manifests in the emergence of plasmons in heated undoped samples [2, 71, 73], as well as plasmon shifts when the electronic temperature is increased [8, 74]. The effects are dramatic at electronic temperatures of a few 1000s K, which can be reached using femtosecond laser pulses without damaging the material [75, 76]. In this context, while SNOM has been extensively used to characterize graphene plasmons [2, 50, 52, 53, 58], the unique combination of space, time, momentum, and energy resolution offered by OPEP makes it an ideal technique to reveal unexplored properties of those excitations, as well as other types of polaritons and their associated electron/lattice dynamics in 2D materials.

Here, we use predictive theory to demonstrate that the ultrafast OPEP approach can be used to characterize the temporal dynamics of plasmons in both extended and nanostructured graphene and graphite films. Specifically, we show that the strong confinement of plasmons in these materials produces large deflection in the inelastically scattered electrons, directly yielding dispersion curves in the energy-momentum-resolved electron transmission maps. Adjustment of the light/electron delay allows us to explore the temporal evolution of these excitations as the material undergoes an initial rapid increase in electronic temperature upon optical pumping, followed by slower cooling through relaxation to the atomic lattice over a subpicosecond timescale. Importantly, for laterally confined plasmons, such as transverse modes in ribbons, there is a strong correlation between plasmon energy and momentum, which enables the identification of these modes by collecting the angle-resolved transmitted electrons integrated over a wide energy window, thus avoiding the need to use a spectrometer. This approach is particularly advantageous to study low-energy modes, where conventional imaging in the Fourier plane of an electron microscope could serve to identify polaritons in a spectral window below the accessible range in currently available setups. The present results should stimulate the use of OPEP to study the ultrafast dynamics of polaritons in materials that possess a strong thermo-optical response, such as graphene and other 2D crystals in extended and nanostructured geometries.

II. THE ULTRAFAST OPTICAL-PUMP/ELECTRON PROBE (OPEP) APPROACH

The electron signal carries spectral information on excitations in the sample, and in addition, the angular distribution of inelastically scattered electrons reveals the spatial characteristics of those excitations. The acquisition

of energy-momentum-resolved maps of transmitted electrons can directly yield dispersion curves of the sample modes [24]. OPEP further adds temporal resolution, as we illustrate in Figure 1. The sample (a graphene ribbon in this example) is optically pumped with an ultrafast laser (Figure 1a), which creates an elevated electronic temperature in the material that is probed at a later time by a delayed electron pulse (Figure 1a). Incidentally, the temperature rise occurs rather early because of the $\sim T_e^3$ scaling of the electronic heat with temperature (see Appendix D). The dynamics of rapid femtosecond heating followed by the subsequent picosecond cooling of graphene electrons is traced through the delay-dependent variations observed in the distribution of scattered electrons, which is represented in Figure 1c for a fixed lost energy using the methods and analysis explained below. Additional plots analogous to Figure 1c are presented in supplementary Figure 5 for different values of the energy loss and for graphite ribbons.

The power of momentum- and energy-resolved OPEP is illustrated in Figure 2 for a self-standing highly-doped extended graphene sample. Figure 2a shows a scheme of the pump-probe configuration, with electrons incident normal to the graphene plane. When excited by an ultrashort optical pulse, high-energy electronic bands of graphene are populated, creating a nonequilibrium distribution of hot electrons, which quickly thermalizes to a high-temperature quasistationary state due to carrier-carrier scattering [12, 76]. During a subpicosecond timescale, the electronic temperature decreases as a result of a cascade of inelastic scattering processes, in particular by emitting and absorbing phonons [78]. Figure 2b shows the temporal evolution of the temperature as modelled through the two-temperature model (see details in Appendix D) for two different optical pump fluences, reaching transient electronic temperatures as high as $T_e \sim 3000$ K. When probed with a delayed quasi-monochromatic electron pulse, the graphene plasmon dispersion can be mapped out from the energy- and angle-resolved inelastically scattered electron distribution. At room temperature (Figure 2c), the dispersion relation is dominated by a plasmon band with a characteristic $\omega \sim \sqrt{k_{\parallel}}$ wave vector-frequency dispersion that is well documented for doped graphene [71] (we use a Fermi energy $E_F = 0.2$ eV throughout this paper, see Appendix A for details of the calculations). Interestingly, negative energy losses (i.e., energy gains) are observed from electrons that absorb thermally populated plasmons (Figure 2c). Energy gains associated with optical phonons were equally observed in a pioneering experiment for electrons traversing thin LiF films [79], and more recently, this approach has been used to determine the phononic temperature in nanostructures [19, 80]. In the present study, the gain dispersion band is resolved in momentum, showing mirror symmetry with respect to the horizontal axis, except for the difference in electron scattering probability, as losses are proportional to $n_{T_e}(\omega) + 1$ and gains to $n_{T_e}(\omega)$, where $n_{T_e}(\omega)$ is the Bose-Einstein distribu-

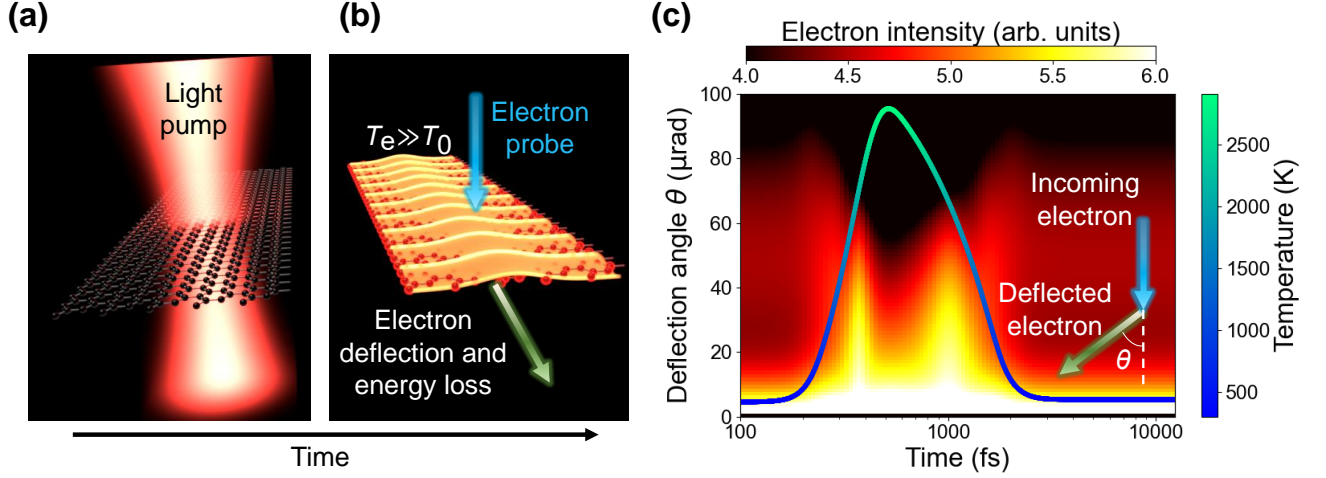


FIG. 1: Schematic illustration of ultrafast optical-pump/electron-probe (OPEP) sampling through energy-momentum transfer. (a) An ultrashort light pulse irradiates the sample at the initial time and elevates its electronic temperature. (b) A delayed electron pulse probes the thermal dynamics of sample excitations, which are revealed by the energy loss and lateral deflection that they produce on the electron, depending on the spatial distribution of those excitations. (c) Following optical pumping, the electron temperature (curve and right scale) first raises rapidly and then decays with time (lower horizontal scale), giving rise to a temporal variation in the inelastic electron scattering probability (density plot) with deflection angle (vertical scale), here represented for a 100 nm wide graphene ribbon (0.2 eV Fermi energy, 4 meV damping) sampled by 100 keV electrons that lose 0.2 eV.

tion at the electron temperature T_e (see Appendix A). At higher temperature (Figure 2d) n_{T_e} increases, thus reducing the relative difference between gain and loss probabilities. Additionally, the plasmon energy undergoes a clearly discernible blue shift because $k_B T_e$ (~ 0.26 eV at $T_e = 3000$ K) exceeds $E_F = 0.2$ eV [81]. We also observe an elevation in plasmon broadening beyond the intrinsic damping ($\hbar\tau^{-1} = 4$ meV) due to the availability of extra electron-hole-pair transitions that become accessible as T_e increases [71]. These conclusions are maintained when examining results for different values of E_F (supplementary Figure 6) and multilayer graphene films (supplementary Figure 7). Incidentally, the fraction of inelastically scattering electrons is rather high at the relatively low plasmon energies under consideration [82], giving rise to plasmon replicas associated with multiple losses (supplementary Figure 8).

A. Revealing lateral plasmon confinement

Ribbons break translational invariance and produce lateral plasmon confinement. We illustrate the resulting discretization in electron deflection in Figure 3, where the momentum- and energy-resolved inelastic scattering cross section $\sigma_{xc}(\mathbf{k}_{\parallel}, \omega)$ is represented for an extended electron beam interacting with cool and heated graphene and graphite ribbons. This quantity is proportional to the loss probability, as explained in the Appendix B. In Figure 3a-e we show calculations for a 100 nm wide graphene ribbon doped to $E_F = 0.2$ eV Fermi energy,

whereas in Figure 3f-j we consider a graphite ribbon of the same width and consisting of 10 monolayers (equivalent to ≈ 3.3 nm thickness) of undoped graphene (i.e., we disregard any residual doping, which should be diluted in a larger number of layers). For graphene, the results for electron deflection in the plane containing the direction of the ribbon translational symmetry (Figure 3d,e) are similar to those for planar graphene (Figure 2), as expected from the similarity between the dispersion relations of the lowest-order monopolar plasmon waveguide in ribbons (see supplementary Figure 9) and plasmons in extended samples [83]. The dipolar waveguide mode, which crosses $\mathbf{k}_{\parallel} = 0$ at finite energy ~ 0.2 eV, is also discernible, particularly at low temperature (Figure 3d), while higher-order modes are not efficiently excited. In contrast, electron deflection along the transverse direction (Figure 3b,c) exhibits sharp spectral features that reveal lateral confinement, accompanied by a milder momentum discretization resulting from the finite cosine-like charge distribution of plasmons across the ribbon. Like in extended graphene, an elevation in temperature produces plasmon blue shifts, an increase in spectral broadening, and a more symmetric gain-loss distribution. For graphite, the situation is different because the sample is undoped, so no plasmons are observed at low temperature (Figure 3g,i), while a broad plasmon feature emerges at 3000 K for electron deflection along the ribbon (Figure 3j), which is quantized in energy for deflection across the ribbon (Figure 3h), again due to lateral confinement. Additional plots offered in supplementary Figures 10, 11, and 12 show the variation of the results in Figure 3 with

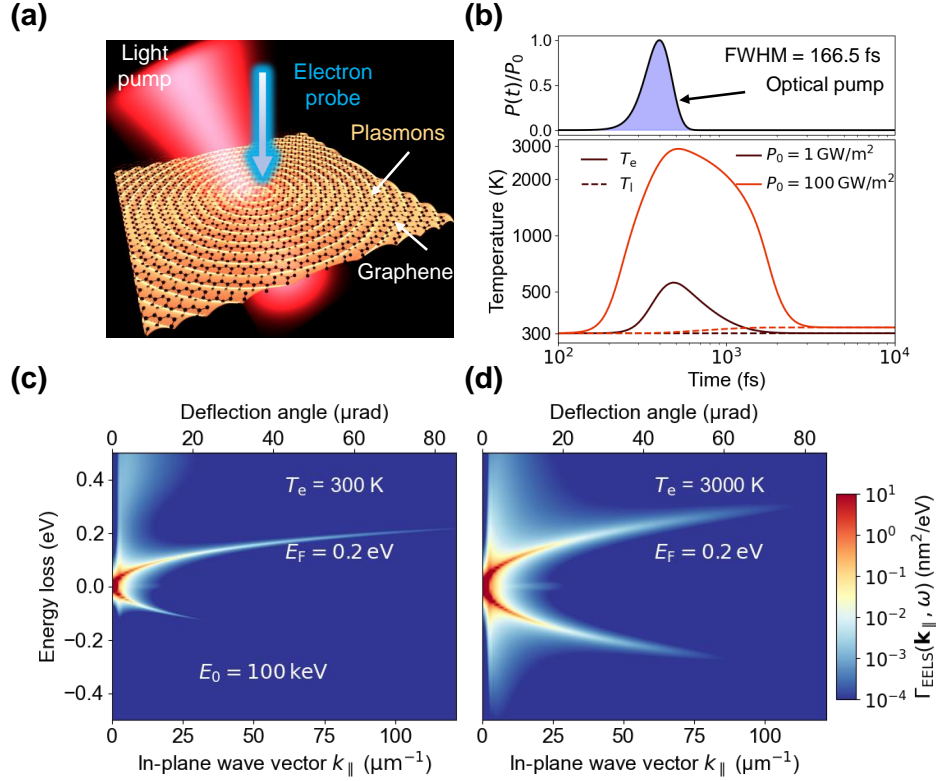


FIG. 2: OPEP characterization of plasmons in extended graphene. (a) Schematic representation of a graphene layer and OPEP configuration, with electrons impinging normal to the plane of the sample. (b) Temporal profiles of the optical-pump absorption (top panel, Gaussian 166.5 fs FWHM, peaked at a time of 400 fs) and sample temperatures (bottom panel). We plot the electron (T_e , solid curves) and lattice (T_l , dashed curves) temperatures in the two-temperature model for two different normal-incidence peak absorption powers ($P_0 = 10^9$ and 10^{11} W/m^2 , pulse fluences of $(0.177/\pi\alpha)$ and $(17.7/\pi\alpha) \text{ mJ/m}^2$, respectively, where $\pi\alpha \approx 0.023$ is the absorbance of free-standing graphene in the visible range[77]). (c, d) Momentum- and energy-resolved loss probability $\Gamma_{\text{EELS}}(\mathbf{k}_{\parallel}, \omega)$ for 100 keV transmitted electrons, revealing features associated with plasmon excitation in the sample for (c) low (300 K) and (d) high (3000 K) electronic temperature regimes. The graphene Fermi energy is $E_F = 0.2 \text{ eV}$ and the intrinsic damping is $\hbar\tau^{-1} = 4 \text{ meV}$ (lifetime $\tau = 164.5 \text{ fs}$).

graphene doping, graphene ribbon width, and graphite thickness, respectively.

B. Spectrometer-free momentum-resolved OPEP

Quantization of momentum transfer due to lateral plasmon confinement suggests the possibility that these excitations and their temporal dynamics can be revealed by integrating the inelastic electron signal over a broad energy range, thus avoiding the need for highly-monochromatic electron beams and precise spectrometers. We explore this idea in Figure 4a,b, where we present the energy-integrated (within the -0.5 eV to 0.5 eV range) cross sections extracted from Figure 3 for electron deflection across the ribbon (i.e., as a function of k_x for $k_y = 0$). The results show clear momentum quantization in the inelastic electron signal, which becomes clearer as the temperature increases, particularly for the graphene ribbon. These observations suggest that the dynamics of the system could also be followed by measuring

the energy-integrated electron angular distribution in the Fourier plane of the electron microscope. The delay-time dependence of the electron signal is shown in Figure 4c,d (density plots), following the evolution of the electronic temperature (curves) in graphene and graphite ribbons upon optical pumping. Our calculations corroborate the increase in the visibility of the oscillations observed in the inelastic scattering probability as a function of deflection angle around the time of maximum heating.

III. CONCLUSION

Besides its fundamental interest, the study of ultrafast thermal dynamics of material excitations opens exciting opportunities for applications in optical switching and light modulation [5]. In this work, we have demonstrated based on solid theoretical calculations that the optical-pump/electron-probe approach, which is becoming accessible within a growing number of ultrafast electron microscope setups, grants us access into nanoscale de-

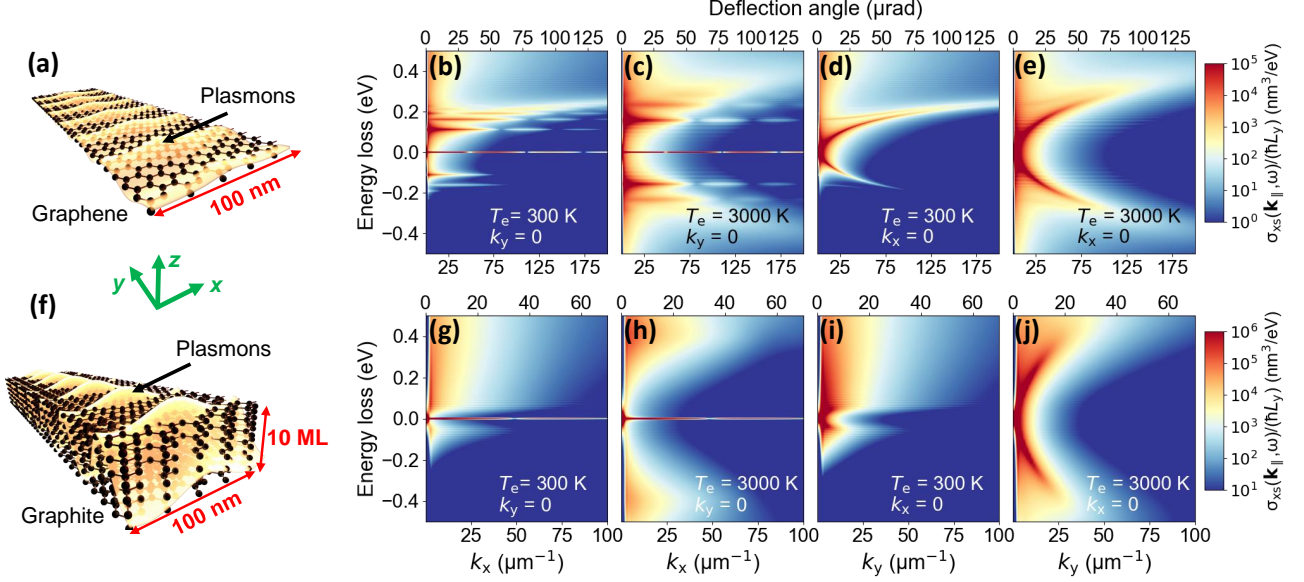


FIG. 3: Quantization of the plasmon lateral momentum in graphene and graphite ribbons characterized by OPEP. (a-e) We plot the energy- and momentum-resolved differential cross section of 100 nm wide graphene ribbons (0.2 eV Fermi energy, 4 meV damping, see sketch in (a)) toward 100 keV electron plane waves as a function of lost energy (vertical scales) and lateral momentum transfer (horizontal scales); we present cuts along both k_x with $k_y = 0$ (b,c) and k_y with $k_x = 0$ (d,e) for two different electronic temperatures T_e (see labels). (f-j) Same as (a-e), but for 100 nm wide, 3.3 nm thick graphite ribbons (equivalent to 10 undoped graphene monolayers (MLs)) with the same intrinsic damping. We represent the momentum- and energy-resolved inelastic electron scattering cross section $\sigma_{xs}(\mathbf{k}_{\parallel}, \omega)$ normalized to the ribbon length L_y (see Appendix B).

tails of such dynamics combined with femtosecond temporal resolution. This method, which brings a radical enhancement in spatial resolution compared to alternative diffraction-limited optical probes, can rely on spectrometer-free momentum-resolved electron detection (i.e., in the microscope Fourier plane) when sampling nanostructures with a well-defined characteristic length, such as the width in ribbons, leading to momentum quantization due to lateral confinement of the supported excitations. In addition, the sampled mode energies can be arbitrarily low, provided their spatial extension is small enough to produce measurable transfers of lateral momentum to the electrons. We have illustrated the power

of this concept by showing that energy-integrated, angle-resolved electron signals can reveal plasmons in structures of ~ 100 nm lateral size, which produce electron deflection angles that are sufficiently large to be resolved by a large fraction of existing transmission electron microscopes. The proposed approach should be generally applicable to study surface excitations in 2D materials, as well as local details of insulator-metal transition in vanadium and indium-titanium oxides, where the electron and lattice dynamics triggered by pumping with ultrafast laser pulses could provide information on collective electronic and vibronic excitations with combined nanometer and femtosecond spatiotemporal resolution.

APPENDIX

Appendix A: Electron energy-loss and -gain probabilities in extended planar films

We follow a well-established formalism [82] to calculate the loss probability of an electron that is normally impinging on a planar thin film. The distribution of transmitted electrons as a function of transferred transverse momentum $\hbar\mathbf{k}_{\parallel}$ and energy $\hbar\omega$ is given by

$$\Gamma_{\text{EELS}}^0(\mathbf{k}_{\parallel}, \omega) = \frac{2e^2}{\hbar\pi^2 v^2} \frac{k_{\parallel}}{(k_{\parallel}^2 + \omega^2/v^2)^2} \text{Im}\{r_p(k_{\parallel}, \omega)\}$$

at zero electronic temperature, where we disregard small retardation effects for simplicity. Here, $r_p(k_{\parallel}, \omega)$ denotes the momentum- and frequency-dependent Fresnel reflection coefficient of the film for p polarization, which is in turn

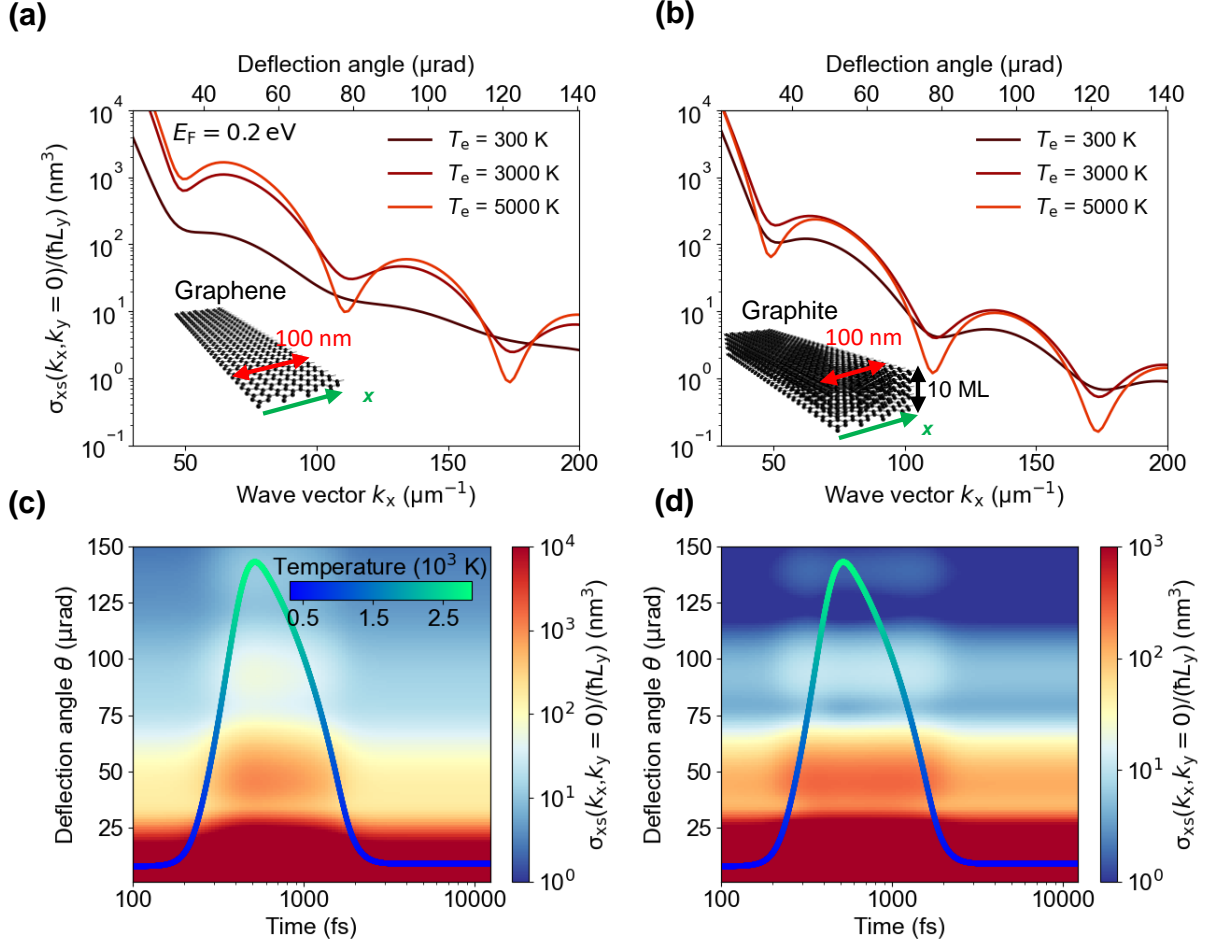


FIG. 4: Demonstration of spectrometer-free momentum-resolved OPEP. We plot the dependence on transverse momentum transfer (lower horizontal axes), or equivalently, deflection angle (upper axes), predicted for the energy-integrated, momentum-resolved inelastic electron cross section $\sigma_{xc}(\mathbf{k}_{\parallel}) = \int d\omega \sigma_{xc}(\mathbf{k}_{\parallel}, \omega)$ for (a,c) doped graphene and (b,d) undoped graphite samples with the same electron temperatures and additional parameters as in Figure 3. The energy integral extends from -0.5 eV to 0.5 eV. We focus on $k_y = 0$ (i.e., electrons scattered within a plane perpendicular to the ribbon axis) and show results (a,b) for selected temperatures and (c,d) for the temporal evolution under optical pumping, with the probability (density plots) and temperature (curves) shown in the same way as in Figure 1b.

expressed in terms of the surface conductivity $\sigma(k_{\parallel}, \omega)$ (see Appendix C) as

$$r_p(k_{\parallel}, \omega) = \frac{1}{1 - i\omega/[2\pi k_{\parallel} \sigma(k_{\parallel}, \omega)]},$$

where we neglect retardation effects. We thus describe the film as a zero-thickness layer under the assumption that the involved surface modes have long wavelengths compared to the film thickness. For graphene, we use the random-phase approximation (RPA) conductivity (see Appendix C), while a thin graphite film consisting of N graphene planes is represented by the graphene conductivity multiplied by N . For finite electronic temperature T_e , the electron energy-loss probability needs to be corrected due to the following two effects: (1) the reflection coefficient is modified by the thermal dependence of the film conductivity (see Appendix C); and (2) the thermal population of excited electronic states in the film produces an increase in energy losses, as well as a finite probability of energy gains, captured by the expression [84, 85]

$$\Gamma_{\text{EELS}}^{T_e}(\mathbf{k}_{\parallel}, \omega) = \Gamma_{\text{EELS}}^0(\mathbf{k}_{\parallel}, |\omega|) [n_{T_e}(\omega) + 1] [\Theta(\omega) - \Theta(-\omega)],$$

where

$$n_{T_e}(\omega) = \frac{1}{e^{\hbar\omega/k_B T_e} - 1}$$

is the frequency- and temperature-dependent Bose-Einstein distribution, the $\Theta(-\omega)$ term accounts for energy gain, and we have used the property $-n_{T_e}(-\omega) = n_{T_e}(\omega) + 1$. In the present work, we apply this model to describe inelastic electron scattering in graphene and few-layer graphite extended films.

Appendix B: Inelastic electron scattering cross section of planar nanostructures

We consider a free electron moving along z and initially prepared in a plane wave state $\psi_i(\mathbf{r}) = e^{ip_{i,z}z}/\sqrt{AL}$ of energy $\hbar\varepsilon_i$ and momentum $\hbar p_{i,z}\hat{\mathbf{z}}$, where A and L are the transverse area and longitudinal length of the quantization box, respectively. The electron is taken to interact with a planar structure lying in the $z = 0$ plane. We aim to calculate the transition probability to a final state $\psi_f(\mathbf{r}) = e^{ip_{f,z}z}e^{i\mathbf{k}_{\parallel}\cdot\mathbf{R}}/\sqrt{AL}$ of energy $\hbar\varepsilon_f$ and momentum $\hbar(\mathbf{k}_{\parallel} + p_{f,z}\hat{\mathbf{z}})$, where \mathbf{k}_{\parallel} is the transverse wave vector transfer and $\mathbf{R} = (x, y)$. Neglecting retardation, the energy-resolved inelastic transition rate is given by [14]

$$\frac{d\Gamma(\omega)}{dt} = \frac{2e^2}{\hbar} \sum_f \int d^3\mathbf{r} \int d^3\mathbf{r}' \psi_f(\mathbf{r}) \psi_i^*(\mathbf{r}) \psi_f^*(\mathbf{r}') \psi_i(\mathbf{r}') \text{Im}\{-W^{\text{ind}}(\mathbf{r}, \mathbf{r}', \omega)\} \delta(\varepsilon_f - \varepsilon_i + \omega),$$

where $W^{\text{ind}}(\mathbf{r}, \mathbf{r}', \omega)$ is the induced part of the screened Coulomb interaction. We now (1) make the substitution $\sum_f \rightarrow AL(2\pi)^{-3} \int d^2\mathbf{k}_{\parallel} \int dp_{f,z}$, (2) adopt the nonrecoil approximation to express the transition frequency as $\varepsilon_i - \varepsilon_f \approx v(p_{i,z} - p_{f,z})$, where v is the electron velocity, and (3) divide the rate $d\Gamma/dt$ by the incident electron current density $v/(AL)$ to obtain the spectrally-resolved inelastic scattering cross section $\sigma_{\text{xc}}(\omega) = \int d^2\mathbf{k}_{\parallel} \sigma_{\text{xc}}(\mathbf{k}_{\parallel}, \omega)$, where

$$\sigma_{\text{xc}}(\mathbf{k}_{\parallel}, \omega) = \frac{e^2}{4\pi^3 \hbar v^2} \int d^3\mathbf{r} \int d^3\mathbf{r}' e^{i\mathbf{k}_{\parallel}\cdot(\mathbf{R}-\mathbf{R}')} e^{i\omega(z'-z)/v} \text{Im}\{-W^{\text{ind}}(\mathbf{r}, \mathbf{r}', \omega)\} \quad (\text{B1})$$

is the cross section resolved in momentum and energy transfers $\hbar\mathbf{k}_{\parallel}$ and $\hbar\omega$.

We describe the planar structure through a local surface conductivity $\sigma(\omega) \equiv \sigma(k_{\parallel} = 0, \omega)$. Using a quasistatic eigenmode expansion detailed elsewhere [82], this allows us to express the screened interaction as

$$W^{\text{ind}}(\mathbf{r}, \mathbf{r}', \omega) = D \sum_j \frac{1}{1/\eta_j - 1/\eta(\omega)} \phi_j(\mathbf{r}) \phi_j(\mathbf{r}') \quad (\text{B2})$$

in terms of size-independent real-valued charge distributions $\rho_j(\boldsymbol{\theta})$ and eigenvalues η_j , where $\eta(\omega) = i\sigma(\omega)/\omega D$,

$$\phi_j(\mathbf{r}) = \int d^2\boldsymbol{\theta} \frac{\rho_j(\boldsymbol{\theta})}{|\mathbf{r} - D\boldsymbol{\theta}|} \quad (\text{B3})$$

are normalized scalar mode potentials, $\boldsymbol{\theta} = \mathbf{R}/D$ is the in-plane position vector \mathbf{R} normalized to the ribbon width D , and j labels different modes (see below). Inserting Eq. (B2) into Eq. (B1), we find

$$\sigma_{\text{xc}}(\mathbf{k}_{\parallel}, \omega) = \frac{e^2 D}{4\pi^3 \hbar v^2} \sum_j \text{Im} \left\{ \frac{1}{1/\eta(\omega) - 1/\eta_j} \right\} |\tilde{\phi}_j(\mathbf{k})|^2 \quad (\text{B4})$$

where $\tilde{\phi}_j(\mathbf{k}) = \int d^3\mathbf{r} e^{i\mathbf{k}\cdot\mathbf{r}} \phi_j(\mathbf{r})$ and $\mathbf{k} = \mathbf{k}_{\parallel} + (\omega/v)\hat{\mathbf{z}}$. Then, using the Fourier transform $4\pi/k^2$ of the Coulomb potential $1/r$ in Eq. (B3), we find $\tilde{\phi}_j(\mathbf{k}) = (4\pi/k^2) \tilde{\rho}_j(\mathbf{k}_{\parallel})$, where

$$\tilde{\rho}_j(\mathbf{k}_{\parallel}) = \int d^2\boldsymbol{\theta} \rho_j(\boldsymbol{\theta}) e^{-i\mathbf{k}_{\parallel}\cdot\boldsymbol{\theta}D}. \quad (\text{B5})$$

This allows us to recast Eq. (B4) as

$$\sigma_{\text{xc}}(\mathbf{k}_{\parallel}, \omega) = \frac{4e^2 D}{\pi \hbar v^2} \frac{1}{(k_{\parallel}^2 + \omega^2/v^2)^2} \sum_j \text{Im} \left\{ \frac{1}{1/\eta(\omega) - 1/\eta_j} \right\} |\tilde{\rho}_j(\mathbf{k}_{\parallel})|^2, \quad (\text{B6})$$

which has units of $\text{time} \times (\text{length})^4$.

Here, we apply this formalism to ribbons of width D that possess translational invariance along y (Figure 3a,b), so it is convenient to multiplex the mode index as $j \rightarrow \{j, q\}$ into a transverse index (we retain j for this purpose) and a wave vector q/D along y . This needs to be accompanied by the substitutions $\sum_j \rightarrow \sum_{jq}$ and $\rho_j(\theta) \rightarrow \rho_{jq}(\theta_x) e^{iq\theta_y} \sqrt{D/L_y}$, where $L_y \gg D$ is the ribbon length and we incorporate the wave-plane dependence on θ_y in the charge distribution. We now rewrite Eq. (B5) as $\tilde{\rho}_j(\mathbf{k}_{\parallel}) \rightarrow \tilde{\rho}_j(\mathbf{k}_{\parallel}) \delta_{q,k_y D} \sqrt{L_y/D}$ by making the reassignment

$$\tilde{\rho}_j(\mathbf{k}_{\parallel}) = \int_{-1/2}^{1/2} d\theta_x \rho_{j,k_y D}(\theta_x) e^{-i\theta_y k_y D}. \quad (\text{B7})$$

Finally, the counterpart of Eq. (B6) for translationally invariant ribbons reduces to

$$\frac{\sigma_{\text{xc}}(\mathbf{k}_{\parallel}, \omega)}{L_y} = \frac{4e^2}{\pi \hbar v^2} \frac{1}{(k_{\parallel}^2 + \omega^2/v^2)^2} \sum_j \text{Im} \left\{ \frac{1}{1/\eta(\omega) - 1/\eta_{j,k_x D}} \right\} |\tilde{\rho}_j(\mathbf{k}_{\parallel})|^2, \quad (\text{B8})$$

which is normalized to the ribbon length L_y and has units of $\text{time} \times (\text{length})^3$. We use Eqs. (B7) and (B8) to calculate the results presented in Figures 3 and 4.

Appendix C: Graphene conductivity at finite temperature

The temperature-dependent nonlocal RPA surface conductivity of graphene is given by [86, 87]

$$\sigma^0(k_{\parallel}, \omega) = \frac{ie^2 \omega}{2\pi^2 \hbar k_{\parallel}^2} \int d^2 \mathbf{q} \sum_{s,s'=\pm 1} \left[1 + ss' \frac{\mathbf{q} \cdot (\mathbf{k}_{\parallel} + \mathbf{q})}{q|\mathbf{k}_{\parallel} + \mathbf{q}|} \right] \frac{n_F(s' \hbar v_F |\mathbf{k}_{\parallel} + \mathbf{q}|) - n_F(s \hbar v_F q)}{\omega - v_F(sq - s'|\mathbf{k}_{\parallel} + \mathbf{q}|) + i0^+}, \quad (\text{C1})$$

where the superscript 0 indicates that inelastic relaxation occurs at an infinitesimal rate, $v_F \approx 10^6 \text{ m/s}$ is the Fermi velocity, T_e is the electronic temperature, $n_F(E) = [e^{(E-\mu)/k_B T_e} + 1]^{-1}$ is the Fermi-Dirac distribution function, and μ is the temperature-dependent chemical potential. The latter can be approximated as [81] $\mu \approx E_F \left[(1 + \xi^2)^{1/2} - \xi \right]^{1/2}$, where $E_F = \hbar v_F \sqrt{\pi n}$ is the zero-temperature Fermi energy for a doping carrier density n , and $\xi = (2 \log^2 4)(k_B T_e/E_F)^2$. At $T_e = 0$, we have $n_F(E) = \Theta(E_F - E)$ and the conductivity admits the analytical expression [86, 87]

$$\sigma_{T_e=0}^0(k_{\parallel}, \omega, E_F) = \frac{-2ie^2 \omega}{\pi \hbar v_F} \left[\frac{k_F}{k_{\parallel}^2} + \frac{[G(\Delta_-) - G(-\Delta_-) + i\pi]\Theta(\text{Re}\{\Delta_-\} + 1) + G(-\Delta_-) - G(\Delta_+)}{8\sqrt{\omega^2/v_F^2 - k_{\parallel}^2}} \right],$$

with $G(z) = z\sqrt{z^2 - 1} - \log(z + \sqrt{z^2 - 1})$ and $\Delta_{\pm} = (\omega/v_F \pm 2k_F)/k_{\parallel}$, where the square root is taken to yield positive real parts and the imaginary part of the log function is taken in the $[-\pi, \pi]$ sheet. As a more efficient alternative to evaluating the integral in Eq. (C1), we calculate the T_e -dependent conductivity from the $T_e = 0$ expression using the identity [88] $n_F(E) = (4k_B T_e)^{-1} \int_{-\infty}^{\infty} dx \Theta(x - E) / \cosh^2[(\mu - x)/(2k_B T_e)]$, which allows us to write

$$\sigma^0(\mathbf{k}_{\parallel}, \omega) = \frac{1}{4k_B T_e} \int_{-\infty}^{\infty} dx \sigma_{T_e=0}^0(k_{\parallel}, \omega, x) \cosh^{-2}\left(\frac{\mu - x}{2k_B T_e}\right).$$

Finally, we introduce a phenomenological inelastic lifetime τ using the Mermin prescription [89]

$$\sigma(\mathbf{k}_{\parallel}, \omega) = \frac{(1 + i/\omega\tau)\sigma^0(\mathbf{k}_{\parallel}, \omega + i/\tau)}{1 + (i/\omega\tau)\sigma^0(\mathbf{k}_{\parallel}, \omega + i/\tau)/\sigma^0(\mathbf{k}_{\parallel}, 0)},$$

which is designed to preserve the local electron density. Although τ exhibits a complex dependence on temperature (see supplementary Figure 13a,b), we adopt for simplicity a constant value given by $\hbar\tau^{-1} = 4 \text{ meV}$ throughout this work. Finally, we note that we describe graphite films consisting of N undoped graphene layers by means of a temperature-dependent surface-conductivity $N\sigma(\mathbf{k}_{\parallel}, \omega)$ evaluated at $E_F = 0$.

Appendix D: Two-temperature model

We ignore thermal diffusion under the assumption that the structures are pumped with spatially homogeneous illumination and further neglect radiative emission in our self-standing samples. Then, for simplicity, we find the time- and position-dependent electronic and lattice temperatures, $T_e(\mathbf{R}, t)$ and $T_l(\mathbf{R}, t)$, by solving a stripped version of the two-temperature model equations [90]

$$\begin{aligned} c_e \frac{dT_e}{dt} &= p^{\text{abs}} + A(T_e^3 - T_l^3), \\ c_l \frac{dT_l}{dt} &= -A(T_e^3 - T_l^3), \end{aligned}$$

where c_e and c_l are the graphene electronic and phononic heat capacities per unit area, $p^{\text{abs}}(\mathbf{R}, t)$ is the absorption power density due to optical pumping, and the rightmost terms account for electron-phonon coupling. We assume that the latter is dominated by disorder, which leads to the $\sim T^3$ scaling [8, 91] with $A = (1.2\mathcal{D}^2|\mu|k_B^3)/(\pi^2\rho\hbar^4v_F^3v_s^2L)$, where $\rho = 7.6 \times 10^{-8}$ g/cm² and $\mathcal{D} \approx 40$ eV are the graphene mass density and deformation potential, respectively, $v_s \approx 0.02 v_F$ is the graphene sound velocity, and $L \approx 10$ nm. The electronic heat capacity $c_e = \partial Q_e / \partial T_e$ is obtained as the derivative of the surface heat density [81] $Q_e = \beta(k_B T_e)^3 / (\hbar v_F)^2$, where $\beta = (2/\pi) \int_0^\infty x^2 dx [(e^{x+\mu/k_B T_e} + 1)^{-1} + (e^{x-\mu/k_B T_e} + 1)^{-1}] - (2/3\pi)(E_F/k_B T_e)^3 = -(4/\pi)[\text{Li}_3(-e^{-\mu/k_B T_e}) + \text{Li}_3(-e^{\mu/k_B T_e})] - (2/3\pi)(E_F/k_B T_e)^3$, where $\text{Li}_n(x) = \sum_{k=1}^\infty x^k/k^n$ is the polylogarithm function of order n . The phonon heat capacity is calculated as [92] $c_l = 9k_B^3 T_l^2 \zeta(3)/(\pi\hbar^2 v_{\text{ph}}^2)$, where $v_{\text{ph}} \approx 10^4$ m/s is the phonon velocity and $\zeta(3) \approx 1.202$ is the Riemann Zeta function; this expression is valid for small T_l compared with the Debye temperature ~ 1000 K in graphene (see Figure 1b). Actually, c_l is several orders of magnitude higher than c_e (see supplementary Figure 13c), which implies that the former plays a minor role and T_l does not increase substantially compared with T_e (see Figure 2b).

Appendix E: Summary of quasistatic eigenmodes for ribbons

We consider a ribbon of width D having translational invariance along y , for which we intend to find mode eigenvalue and eigenfunctions η_s and $\tilde{\rho}_j(\mathbf{k}_\parallel)$, where $\mathbf{k}_\parallel = (k_x, k_y)$ and we use the combined mode index $s = \{j, q = k_y D\}$. This problem has been addressed using different methods, including electromagnetic simulations [51], direct solution of the associated self-consistent quasistatic integral equation [93, 94], and inversion of the corresponding integral eigenvalue problem in real-space and special-function representations of the mode fields [82, 95–97]. Here, we find fast convergence in the solution of the eigenvalue problem by using a Chebyshev expansion of the electric field, as shown in detail in Appendix F, which yields the following result for the Fourier transform of the mode charge density (see Eq. (B7)):

$$\tilde{\rho}_j(\mathbf{k}_\parallel) = \frac{\pi^2}{2} \sum_{n=0}^\infty (-i)^{n-1} \left\{ 4(n+1)u_{s,n}J_{n+1}\left(\frac{k_x D}{2}\right) - ik_y D v_{s,n} \left[J_n\left(\frac{k_x D}{2}\right) + J_{n+2}\left(\frac{k_x D}{2}\right) \right] \right\},$$

where J_n is a Bessel function of order n , and $u_{s,n}$, $v_{s,n}$, and η_s (see tabulated values in supplementary Figure 9a and Tables I and II) are determined from the eigensolutions of the $2N \times 2N$ matrix equation

$$\frac{1}{\eta_s} \begin{bmatrix} \mathcal{A} & 0 \\ 0 & \mathcal{A} \end{bmatrix} \cdot \begin{bmatrix} \mathbf{u}_s \\ \mathbf{v}_s \end{bmatrix} = \begin{bmatrix} \mathcal{M}^{11} & \mathcal{M}^{12} \\ \mathcal{M}^{21} & \mathcal{M}^{22} \end{bmatrix} \cdot \begin{bmatrix} \mathbf{u}_s \\ \mathbf{v}_s \end{bmatrix}, \quad (\text{E1})$$

with $\mathbf{u}_s = [u_{s,0} \cdots u_{s,N-1}]^T$ and $\mathbf{v}_s = [v_{s,0} \cdots v_{s,N-1}]^T$ (T stands for transpose). Matrices in Eq. (F5) are defined in terms of $N \times N$ blocks with coefficients

$$\begin{aligned} \mathcal{A}_{ij} &= U_j(t_i) \sqrt{1 - t_i^2}, \\ \mathcal{M}_{ij}^{11} &= 4 \sum_{m=0}^\infty \left[D_m^{(0)}(0, q, t_i) F_{mj}^{(1)}(t_i) - 2D_m^{(1)}(0, q, t_i) F_{mj}^{(2)}(t_i) - D_m^{(2)}(0, q, t_i) F_{mj}^{(3)}(t_i) + K_m^{(2)}(q, t_i) F_{mj}^{(4)} \right], \\ \mathcal{M}_{ij}^{12} &= -\mathcal{M}_{ij}^{21} = 2q \sum_{m=0}^\infty \left[-D_m^{(0)}(0, q, t_i) F_{mj}^{(2)}(t_i) - D_m^{(1)}(0, q, t_i) F_{mj}^{(3)}(t_i) + K_m^{(1)}(q, t_i) F_{mj}^{(4)} \right], \\ \mathcal{M}_{ij}^{22} &= -q^2 \sum_{m=0}^\infty \left[-D_m^{(0)}(0, q, t_i) F_{mj}^{(3)}(t_i) + K_m^{(0)}(q, t_i) F_{mj}^{(4)} \right], \end{aligned}$$

where $t_i = \cos[\pi(i+1)/(N+1)]$, the indices i and j run from 0 to $N-1$,

$$\begin{aligned}
K_m^{(n)}(q, t) &= [\log(q/4) + \gamma] D_m^{(n)}(0, q, t) + 2 \sum_{k=1}^{\infty} \frac{1}{k} D_m^{(n)}(k, q, t), \quad \text{with } n = 0, 1, 2, \\
D_m^{(0)}(l, q, t) &= \sum_{k=-\infty}^{\infty} (-1)^k C_m(k+2l, q) I_k(qt/2), \\
D_m^{(1)}(l, q, t) &= -\frac{q}{4} \sum_{k=-\infty}^{\infty} (-1)^k [C_m(k+2l+1, q) + C_m(k+2l-1, q)] I_k(qt/2), \\
D_m^{(2)}(l, q, t) &= \frac{q^2}{16} \sum_{k=-\infty}^{\infty} (-1)^k [C_m(k+2l+2, q) + 2C_m(k+2l, q) + C_m(k+2l-2, q)] I_k(qt/2), \\
C_n(\nu, q) &= i^{-\nu} (2 - \delta_{n0}) I_{(n+\nu)/2}(q/4) I_{(n-\nu)/2}(q/4) \times \begin{cases} \cos(\pi\nu/2), & \text{for even } n, \\ i \sin(\pi\nu/2), & \text{for odd } n, \end{cases}
\end{aligned}$$

I_n is a modified Bessel function of order n ,

$$\begin{aligned}
F_{mp}^{(1)}(t) &= -\frac{\pi}{2} [(p+m+1)U_{p+m}(t) + (p-m+1)U_{|p-m+1|-1}(t)], \\
F_{mp}^{(2)}(t) &= \frac{\pi}{2} [T_{p+m+1}(t) + (-1)^{p-m+1}T_{|p-m+1|}(t)], \\
F_{mp}^{(3)}(t) &= \frac{-\pi}{4} [L_{p+m}(t) + L_{|m-p|}(t) - L_{m+p+2}(t) - L_{|m-p-2|}(t)], \\
F_{mp}^{(4)} &= \frac{\pi}{4} (1 - \delta_{m0}) (\delta_{mp} - \delta_{mp+2}),
\end{aligned}$$

$T_n(t)$ and $U_n(t)$ are Chebyshev polynomials (defined by $T_n(\cos \theta) = \cos(n\theta)$ and $U_n(\cos \theta) = \sin[(n+1)\theta]/\sin \theta$), $L_0(t) = T_0(t) \log 2$, and $L_{m>0} = T_m(t)/m$.

The eigenvectors \mathbf{u}_s and \mathbf{v}_s must be normalized in such a way that the mode electric fields satisfy $\int_{-1/2}^{1/2} d\theta_x [\mathcal{E}_{sx}(\theta_x) \mathcal{E}_{s'x}^*(\theta_x) + \mathcal{E}_{sy}(\theta_x) \mathcal{E}_{s'y}^*(\theta_x)] = \delta_{ss'}$ (with $q = q'$), where $\theta_x = x/D$ and

$$\begin{aligned}
\mathcal{E}_{sx}(\theta_x) &= \sum_{n=0}^{\infty} u_{s,n} \sqrt{1-4\theta_x} U_n(2\theta_x), \\
\mathcal{E}_{sy}(\theta_x) &= -i \sum_{n=0}^{\infty} v_{s,n} \sqrt{1-4\theta_x} U_n(2\theta_x)
\end{aligned}$$

are the x and y components of the electric field of mode $s = \{j, q\}$.

Appendix F: Detailed derivation of a solution of quasistatic ribbon plasmon eigenfunctions through the Chebyshev expansion method

We use a Chebyshev polynomial expansion of the optical electric field to calculate semi-analytically the plasmonic eigenmodes of a graphene ribbon of width D lying on the $z = 0$ plane and having translational invariance along y . The ribbon is taken to occupy the $-D/2 < x < D/2$ region. We describe graphene by means of a local, frequency-dependent surface conductivity $\sigma(\omega)$ and incorporate the dependence on surface position $\mathbf{R} = (x, y)$ by writing $\sigma(\mathbf{R}, \omega) = \sigma(\omega) f(\mathbf{R})$, where $f(\mathbf{R}) = 1$ if $|x| \leq D/2$ and 0 otherwise. The monochromatic optical electric field $\mathbf{E}(\mathbf{R}, \omega)$ in the graphene plane then satisfies the integral equation [82]

$$\mathbf{E}(\mathbf{R}, \omega) = \mathbf{E}^{\text{ext}}(\mathbf{R}, \omega) + \frac{i\sigma(\omega)}{\bar{\epsilon}\omega} \nabla_{\mathbf{R}} \int \frac{d^2\mathbf{R}'}{|\mathbf{R} - \mathbf{R}'|} \nabla_{\mathbf{R}'} f(\mathbf{R}') \cdot \mathbf{E}(\mathbf{R}', \omega), \quad (\text{F1})$$

where $\bar{\epsilon}$ is the average permittivity of the embedding medium (see below). Following Ref. 82, we define dimensionless coordinates $\boldsymbol{\theta} = \mathbf{R}/D$ and the normalized electric field $\tilde{\mathcal{E}}(\boldsymbol{\theta}) = D\sqrt{f(\boldsymbol{\theta})}\mathbf{E}$ to rewrite Eq. (F1) as

$$\tilde{\mathcal{E}}(\boldsymbol{\theta}, \omega) = \tilde{\mathcal{E}}^{\text{ext}}(\boldsymbol{\theta}, \omega) + \eta(\omega) \int d^2\boldsymbol{\theta}' \mathbf{M}(\boldsymbol{\theta}, \boldsymbol{\theta}') \cdot \tilde{\mathcal{E}}(\boldsymbol{\theta}', \omega),$$

where

$$\mathbf{M}(\boldsymbol{\theta}, \boldsymbol{\theta}') = \sqrt{f(\boldsymbol{\theta})f(\boldsymbol{\theta}')} \nabla_{\boldsymbol{\theta}} \otimes \nabla_{\boldsymbol{\theta}'} \frac{1}{|\boldsymbol{\theta} - \boldsymbol{\theta}'|}$$

and

$$\eta(\omega) = \frac{i\sigma(\omega)}{D\omega\epsilon}.$$

In the absence of an external field, the above equation reduces to an eigenvalue problem:

$$\vec{\mathcal{E}}_j(\boldsymbol{\theta}, \omega) = \eta_j \int d^2\boldsymbol{\theta}' \mathbf{M}(\boldsymbol{\theta}, \boldsymbol{\theta}') \cdot \vec{\mathcal{E}}_j(\boldsymbol{\theta}', \omega). \quad (\text{F2})$$

Since the kernel \mathbf{M} is real and symmetric, we can find a complete set of orthonormal solutions $\vec{\mathcal{E}}_j$ that satisfy

$$\begin{aligned} \int d^2\boldsymbol{\theta} \vec{\mathcal{E}}_j(\boldsymbol{\theta}) \cdot \vec{\mathcal{E}}_{j'}^*(\boldsymbol{\theta}) &= \delta_{jj'}, \\ \sum_j \vec{\mathcal{E}}_j(\boldsymbol{\theta}) \otimes \vec{\mathcal{E}}_j(\boldsymbol{\theta}') &= \delta(\boldsymbol{\theta} - \boldsymbol{\theta}') \mathbb{I}_{2 \times 2}, \end{aligned}$$

where $\mathbb{I}_{2 \times 2}$ is the 2×2 unit matrix.

We now focus on the specific geometry of a graphene ribbon of width D . Considering its translational invariance along y , we can multiplex the mode index j into a normalized wave vector $q = k_y D$ and the mode order for each fixed value of q (we also use j for the mode order). The spatial dependence of mode $s \equiv \{j, q\}$ is thus given by

$$\vec{\mathcal{E}}_{jq}(\theta_x) e^{iq\theta_y}.$$

Using this, Eq. (F2) can be recast as

$$\vec{\mathcal{E}}_s(\theta_x) = 2\eta_s \int_{-1/2}^{1/2} d\theta'_x (\nabla_{\boldsymbol{\theta}} \otimes \nabla_{\boldsymbol{\theta}'} K_0(q|\theta_x - \theta'_x|) \cdot \vec{\mathcal{E}}_s(\theta'_x), \quad (\text{F3})$$

where $\nabla_{\boldsymbol{\theta}} = \partial_{\theta_x} \hat{\mathbf{x}} + iq\hat{\mathbf{y}}$ and we have made use of the identity

$$\int d\theta'_y e^{iq\theta_y} / |\boldsymbol{\theta} - \boldsymbol{\theta}'| = 2K_0(q|\theta_x - \theta'_x|).$$

Now, the integral equation (F3) can be written in the form

$$\frac{1}{\eta_s} \begin{bmatrix} \mathcal{E}_{sx}(\theta_x) \\ i\mathcal{E}_{sy}(\theta_x) \end{bmatrix} = 2 \int_{-1/2}^{1/2} d\theta'_x \begin{bmatrix} \partial_{\theta_x}^2 & -q\partial_{\theta_x} \\ q\partial_{\theta_x} & -q^2 \end{bmatrix} K_0(q|\theta_x - \theta'_x|) \begin{bmatrix} \mathcal{E}_{sx}(\theta'_x) \\ i\mathcal{E}_{sy}(\theta'_x) \end{bmatrix}.$$

To apply the Chebyshev expansion method, it is convenient to map the integration domain onto the $[-1, 1]$ interval by introducing the variable changes $2\theta_x = t$ and $2\theta'_x = t'$:

$$\frac{1}{\eta_s} \begin{bmatrix} \mathcal{E}_{sx}(t) \\ i\mathcal{E}_{sy}(t) \end{bmatrix} = 4 \int_{-1}^1 dt' \begin{bmatrix} \partial_t^2 & (q/2)\partial_t \\ -(q/2)\partial_t & -(q/2)^2 \end{bmatrix} K_0(q|t - t'|/2) \begin{bmatrix} \mathcal{E}_{sx}(t') \\ i\mathcal{E}_{sy}(t') \end{bmatrix}. \quad (\text{F4})$$

The essence of the Chebyshev method lies on the expansion of the kernel function $K_0(q|t - t'|/2)$ in terms of the Chebyshev polynomials $T_n(t)$ and $U_n(t)$, defined such that $T_n(\cos \theta) = \cos(n\theta)$ and $U_n(\cos \theta) = \sin[(n+1)\theta]/\sin \theta$ [98]. In order to do so, we recall that the modified Bessel function K_0 can be expanded into the Neumann series [99]

$$K_0(z) = -[\ln(z/2) + \gamma] I_0(z) + \sum_{k=1}^{\infty} \frac{2}{k} I_{2k}(z),$$

where $\gamma \approx 0.57721$ is the Euler constant and I_n denotes the modified Bessel function of order n . In addition, one can use the Neumann addition formula for even-order I_{2l}

$$I_{2l}(q|t - t'|/2) = \sum_{k=-\infty}^{\infty} (-1)^k I_{2l+k}(qt'/2) I_k(qt/2)$$

to represent the kernel function as a separable product of functions with arguments t' and t . The other kernel functions in Eq. (F4) can be obtained by taking the first- and second-order derivatives of the above identity with respect to t :

$$\begin{aligned}\frac{\partial}{\partial t} I_{2l}(q|t-t'|/2) &= -\frac{q}{4} \sum_{k=-\infty}^{\infty} (-1)^{k+1} [I_{k+2l-1}(qt'/2) + I_{k+2l-1}(qt/2)] I_k(qt/2), \\ \frac{\partial^2}{\partial t^2} I_{2l}(q|t-t'|/2) &= \frac{q^2}{16} \sum_{k=-\infty}^{\infty} (-1)^k [I_{k-2}(qt/2) + 2I_k(qt/2) + I_{k+2}(qt/2)] I_{k+2l}(qt'/2).\end{aligned}$$

Additionally, the modified Bessel functions can be expanded in a Chebyshev series as [100]

$$\begin{aligned}I_{\nu}(ax) &= \sum_{n=0}^{\infty} C_n(\nu, a) T_n(x), \\ C_n(\nu, a) &= i^{n-\nu} \epsilon_n \varphi_n(\nu) I_{\frac{n+\nu}{2}}\left(\frac{a}{2}\right) I_{\frac{n-\nu}{2}}\left(\frac{a}{2}\right),\end{aligned}$$

with $\epsilon_n = 2 - \delta_{n0}$ and

$$\varphi_n(\nu) = \begin{cases} (-1)^{n/2} \cos(\pi\nu/2), & \text{for even } n, \\ (-1)^{(n-1)/2} \sin(\pi\nu/2), & \text{for odd } n. \end{cases}$$

Using these results, we can readily expand the even-order modified Bessel functions and its derivatives in terms of Chebyshev polynomials T_m as

$$\begin{aligned}I_{2l}(q|t-t'|/2) &= \sum_{m=0}^{\infty} D_m^{(0)}(l, q, t) T_m(t'), \\ \frac{\partial}{\partial t} I_{2l}(q|t-t'|/2) &= \sum_{m=0}^{\infty} D_m^{(1)}(l, q, t) T_m(t'), \\ \frac{\partial^2}{\partial t^2} I_{2l}(q|t-t'|/2) &= \sum_{m=0}^{\infty} D_m^{(2)}(l, q, t) T_m(t'),\end{aligned}$$

where the expansion coefficients are defined as

$$\begin{aligned}D_m^{(0)}(l, q, t) &= \sum_{k=-\infty}^{\infty} (-1)^k C_m(k+2l, q) I_k(qt/2), \\ D_m^{(1)}(l, q, t) &= -\frac{q}{4} \sum_{k=-\infty}^{\infty} (-1)^k [C_m(k+2l+1, q) + C_m(k+2l-1, q)] I_k(qt/2), \\ D_m^{(2)}(l, q, t) &= \frac{q^2}{16} \sum_{k=-\infty}^{\infty} (-1)^k [C_m(k+2l+2, q) + 2C_m(k+2l, q) + C_m(k+2l-2, q)] I_k(qt/2).\end{aligned}$$

Finally, we can obtain the Chebyshev expansion of the functions in the kernel of the integral equation in Eq. (F4) as

$$\begin{aligned}K_0(q|t-t'|/2) &= \sum_{m=0}^{\infty} \left[-\ln|t-t'| D_m^{(0)}(0, q, t) + K_m^{(0)}(q, t) \right] T_m(t'), \\ \frac{\partial}{\partial t} K_0(q|t-t'|/2) &= \sum_{m=0}^{\infty} \left[-\frac{1}{t-t'} D_m^{(0)}(0, q, t) - \ln|t-t'| D_m^{(1)}(0, q, t) + K_m^{(1)}(q, t) \right] T_m(t'), \\ \frac{\partial^2}{\partial t^2} K_0(q|t-t'|/2) &= \sum_{m=0}^{\infty} \left[\frac{1}{(t-t')^2} D_m^{(0)}(0, q, t) - \frac{2}{t-t'} D_m^{(1)}(0, q, t) - \ln|t-t'| D_m^{(2)}(0, q, t) + K_m^{(2)}(q, t) \right] T_m(t'),\end{aligned}$$

where we have defined the quantities

$$\begin{aligned}K_m^{(n)}(q, t) &= \sum_{k=0}^{\infty} \zeta_k(q) D_m^{(n)}(k, q, t), \quad \text{for } n = 0, 1, 2, \\ \zeta_k(q) &= \begin{cases} -[\ln(q/4) + \gamma], & k = 0, \\ 2/k, & \text{otherwise.} \end{cases}\end{aligned}$$

It is also convenient to expand the solutions for \mathcal{E}_{sx} and \mathcal{E}_{sy} in terms of the Chebyshev polynomials $U_n(t)$ as

$$\begin{bmatrix} \mathcal{E}_{sx}(t) \\ i\mathcal{E}_{sy}(t) \end{bmatrix} = \sum_{n=0}^{\infty} \sqrt{1-t^2} U_n(t) \begin{bmatrix} u_{s,n} \\ v_{s,n} \end{bmatrix},$$

which allows us to rewrite Eq. (F4) in the form

$$\frac{1}{\eta_s} \sum_{n=0}^{\infty} \sqrt{1-t^2} U_n(t) \begin{bmatrix} u_{s,n} \\ v_{s,n} \end{bmatrix} = \sum_{p=0}^{\infty} \int_{-1}^1 \begin{bmatrix} 4\partial_t^2 & 2q\partial_t \\ -2q\partial_t & -q^2 \end{bmatrix} K_0(q|t-t'|/2) \sqrt{1-t'^2} U_p(t') \begin{bmatrix} u_{s,p} \\ v_{s,p} \end{bmatrix} dt'.$$

Using the identities

$$\begin{aligned} R_{mp} &= \int_{-1}^1 \frac{T_m(t')T_p(t')}{\sqrt{1-t'^2}} dt' = \begin{cases} \pi, & m=p=0, \\ \frac{\pi}{2}\delta_{mp}, & m \neq 0, p \neq 0, \end{cases} \\ L_m(t) &= \int_{-1}^1 \ln|t-t'| \frac{T_m(t')}{\sqrt{1-t'^2}} dt' = -\pi T_m(t) \begin{cases} \ln(2), & m=0, \\ 1/m, & m \neq 0, \end{cases} \\ S_m &= \text{sign}\{m\}, \end{aligned}$$

as well as the integration properties of the Chebyshev polynomials, after some algebra, we find the results

$$\begin{aligned} F_{mp}^{(1)}(t) &= \int_{-1}^1 \sqrt{1-t'^2} \frac{T_m(t')U_p(t')}{(t-t')^2} dt' = -\frac{\pi}{2} [(p+m+1)U_{p+m}(t) + (p-m+1)U_{|p-m+1|-1}(t)], \\ F_{mp}^{(2)}(t) &= \int_{-1}^1 \sqrt{1-t'^2} \frac{T_m(t')U_p(t')}{(t-t')} dt' = \frac{\pi}{2} [T_{p+m+1}(t) + S_{p-m+1}T_{|p-m+1|}(t)], \\ F_{mp}^{(3)}(t) &= \int_{-1}^1 \ln|t-t'| \sqrt{1-t'^2} T_m(t')U_p(t') dt' = \frac{1}{4} [L_{p+m}(t) + L_{|m-p|}(t) - L_{m+p+2}(t) - L_{|m-p-2|}(t)], \\ F_{mp}^{(4)} &= \int_{-1}^1 \sqrt{1-t'^2} T_m(t')U_p(t') dt' = \frac{1}{2} [R_{m,p} - R_{m,p+2}]. \end{aligned}$$

With this notation, the integral eigenvalue problem reduces to

$$\frac{1}{\eta_s} \sum_{n=0}^{\infty} U_n(t) \sqrt{1-t^2} \begin{bmatrix} u_{s,n} \\ v_{s,n} \end{bmatrix} = \sum_{p=0}^{\infty} \begin{bmatrix} M_p^{11}(q, t) & M_p^{12}(q, t) \\ M_p^{21}(q, t) & M_p^{22}(q, t) \end{bmatrix} \begin{bmatrix} u_{s,p} \\ v_{s,p} \end{bmatrix},$$

where we introduced the definitions

$$\begin{aligned} M_p^{11}(q, t) &= 4 \sum_{m=0}^{\infty} \left[D_m^{(0)}(0, q, t) F_{mp}^{(1)}(t) - 2D_m^{(1)}(0, q, t) F_{mp}^{(2)}(t) - D_m^{(2)}(0, q, t) F_{mp}^{(3)}(t) + K_m^{(2)}(q, t) F_{mp}^{(4)} \right], \\ M_p^{12}(q, t) &= 2q \sum_{m=0}^{\infty} \left[-D_m^{(0)}(0, q, t) F_{mp}^{(2)}(t) - D_m^{(1)}(0, q, t) F_{mp}^{(3)}(t) + K_m^{(1)}(q, t) F_{mp}^{(4)} \right], \\ M_p^{21}(q, t) &= -M_p^{12}(q, t), \\ M_p^{22}(q, t) &= -q^2 \sum_{m=0}^{\infty} \left[-D_m^{(0)}(0, q, t) F_{mp}^{(3)}(t) + K_m^{(0)}(q, t) F_{mp}^{(4)} \right]. \end{aligned}$$

This eigenvalue problem can be recast as a generalized matrix eigenvalue problem if we choose a set of N collocation points $t_l = \cos[\pi(l+1)/(N+1)]$ with $l = 0, \dots, (N-1)$. After doing so, we can write

$$\frac{1}{\eta_s} \begin{bmatrix} \mathcal{A} & \mathbf{0} \\ \mathbf{0} & \mathcal{A} \end{bmatrix} \cdot \begin{bmatrix} \mathbf{u}_s \\ \mathbf{v}_s \end{bmatrix} = \begin{bmatrix} \mathcal{M}^{11} & \mathcal{M}^{12} \\ \mathcal{M}^{21} & \mathcal{M}^{22} \end{bmatrix} \cdot \begin{bmatrix} \mathbf{u}_s \\ \mathbf{v}_s \end{bmatrix}, \quad (\text{F5})$$

where $\mathbf{u}_s = [u_{s,0} \ \dots \ u_{s,N-1}]^T$, $\mathbf{v}_s = [v_{s,0} \ \dots \ v_{s,N-1}]^T$ (the superscript T indicates the transpose),

$$\mathcal{A} = \begin{bmatrix} U_0(t_0)\sqrt{1-t_0^2} & \dots & U_{N-1}(t_0)\sqrt{1-t_0^2} \\ \vdots & & \vdots \\ U_0(t_{N-1})\sqrt{1-t_{N-1}^2} & \dots & U_{N-1}(t_{N-1})\sqrt{1-t_{N-1}^2} \end{bmatrix},$$

$$\mathcal{M}^{\alpha\beta} = \begin{bmatrix} M_0^{\alpha\beta}(q, t_0) & \cdots & M_{N-1}^{\alpha\beta}(q, t_0) \\ \vdots & & \vdots \\ M_0^{\alpha\beta}(q, t_{N-1}) & \cdots & M_{N-1}^{\alpha\beta}(q, t_{N-1}) \end{bmatrix}$$

for $\alpha\beta \in \{11, 12, 21, 22\}$, and $\mathbf{0}$ is a $N \times N$ zero matrix.

The eigenvalues η_s and eigenvectors \mathbf{u}_s and \mathbf{v}_s can be readily found from Eq. (F5) using standard numerical algebra methods. In general, these methods yield orthonormal eigenvectors with elements \tilde{u}_s and \tilde{v}_s (we add the tilde here to clarify that these are the orthonormal eigenvectors that come directly from the eigenvalue equation) that obey the property

$$\sum_{n=0}^{N-1} (\tilde{u}_{s,n}^* \tilde{u}_{s',n} + \tilde{v}_{s,n}^* \tilde{v}_{s',n}) = \delta_{jj'},$$

where $s = \{j, q\}$ and $s' = \{j', q\}$ (i.e., we are dealing with a fixed value of q). However, we note that it is convenient to normalize the obtained eigenvectors in a way that ensures the orthonormality conditions of the fields \mathcal{E}_{sx} and \mathcal{E}_{sy} . This can be done by dividing the eigenvectors \tilde{u}_s and \tilde{v}_s by a factor $\sqrt{A_s}$ with

$$A_s = \sum_{m=0}^{N-1} \sum_{n=0}^{N-1} U_{mn} (\tilde{u}_{s,m}^* \tilde{u}_{s,n} + \tilde{v}_{s,m}^* \tilde{v}_{s,n}),$$

$$U_{mn} = \begin{cases} 0, & |m-n| = 1, \\ \frac{(1+m)(1+n)(1+(-1)^{m+n})}{(1-m+n)(1+m-n)(1+m+n)(3+m+n)}, & \text{otherwise.} \end{cases}$$

In this way, the orthonormality of the fields is ensured, so we have

$$\int_{-1/2}^{1/2} d\theta_x [\vec{\mathcal{E}}_s^*(\theta_x) \cdot \vec{\mathcal{E}}_{s'}(\theta_x)] = \sum_{m=0}^{N-1} \sum_{n=0}^{N-1} U_{mn} (u_{s,m}^* u_{s',n} + v_{s,m}^* v_{s',n}) = \delta_{jj'},$$

where $u_{s,n} = \tilde{u}_{s,n}/\sqrt{A_s}$ and $v_{s,n} = \tilde{v}_{s,n}/\sqrt{A_s}$.

After the expansion coefficients are found, the fields and related physical quantities can be computed analytically. We present a set of numerically obtained eigenvalues and eigenvectors in Tables I-II below. We also show in supplementary Figure 9 the q -dependence of the first six modes of η_s , as well as the spatial profile of the charge distribution and the associated electric fields for the first three modes and different values of q . Once the eigenvectors are normalized, we can also obtain the total charge density of the j^{th} mode in the ribbon as $\rho_s(\boldsymbol{\theta}) = \rho_s(\theta_x) e^{iq\theta_y}$, where the q -dependent $\rho_s(\theta_x)$ function is given by

$$\rho_s(\theta_x) = \sum_{n=0}^{N-1} \left[-2u_{s,n}(n+1) \frac{T_{n+1}(2\theta_x)}{\sqrt{1-4\theta_x^2}} + qv_{s,n} \sqrt{1-4\theta_x^2} U_n(2\theta_x) \right].$$

The Fourier transform of $\rho_s(\boldsymbol{\theta})$, as a function of $\mathbf{k}_{\parallel} = k_x \hat{\mathbf{x}} + k_y \hat{\mathbf{y}}$, can finally be computed analytically, yielding

$$\tilde{\rho}_j(\mathbf{k}_{\parallel}) = \frac{\pi^2}{2} \sum_{n=0}^{\infty} (-i)^{n-1} \left\{ 4(n+1) u_{j,k_y D,n} J_{n+1} \left(\frac{k_x D}{2} \right) - i(k_y D) v_{j,k_y D,n} \left[J_n \left(\frac{k_x D}{2} \right) + J_{n+2} \left(\frac{k_x D}{2} \right) \right] \right\}.$$

Given a certain surface conductivity of the ribbons, $\sigma(\omega)$, we can use the obtained eigenvalues to calculate the dispersion relation of the plasmonic modes by numerically solving the equation [83]

$$-\eta_s = \chi \frac{\text{Im}\{\sigma(\omega)\}}{\bar{\epsilon} \omega D},$$

where $\bar{\epsilon} = (\epsilon_{\text{top}} + \epsilon_{\text{bot}})/2$ is the average permittivity of the materials above and below the ribbon, and we neglect inelastic losses. Considering for simplicity the Drude conductivity

$$\sigma(\omega) = \frac{e^2}{\pi \hbar^2} \frac{iE_F}{\omega + i\gamma},$$

defined in terms of the Fermi energy E_F and a phenomenological inelastic decay rate $\gamma \ll \omega$, the dispersion relation admits the solution

$$\omega_p^{(s)} = \frac{e}{\hbar} \frac{1}{\sqrt{\pi(-\eta_s)}} \sqrt{\frac{E_F}{D}}. \quad (\text{F6})$$

We represent the resulting dispersion relations of the first six plasmon modes of the graphene ribbon in supplementary Figure 9.

Appendix G: Multiple plasmon exchanges in extended films

Two-plasmon exchanges can be approximately described through the relation

$$\Gamma_{\text{EELS}}^{(2)}(\mathbf{k}_{\parallel}, \omega) \approx \Gamma_{\text{EELS}}^{(1)}(\mathbf{k}_{\parallel}, \omega) + \frac{1}{2} \int d^2 \mathbf{k}'_{\parallel} \int d\omega' \Gamma_{\text{EELS}}^{(1)}(\mathbf{k}_{\parallel} - \mathbf{k}'_{\parallel}, \omega - \omega') \Gamma_{\text{EELS}}^{(1)}(\mathbf{k}'_{\parallel}, \omega'), \quad (\text{G1})$$

where

$$\Gamma_{\text{EELS}}^{(1)}(k_{\parallel}, \omega) = \frac{2e^2}{\hbar \pi^2 v^2} \frac{k_{\parallel}}{(k_{\parallel}^2 + \omega^2/v^2)^2} \text{Im}\{r_p(k_{\parallel}, \omega)\} [n_{T_e}(\omega) + 1] \quad (\text{G2})$$

is the single-plasmon interaction probability presented in the Methods section and involving the Bose-Einstein distribution function $n_{T_e}(\omega)$ at the electronic temperature T_e . The integral in Eq. (G1) is computationally demanding, so we simplify it by using the plasmon-pole approximation to the reflection coefficient [101]

$$r_p(k_{\parallel}, \omega) \approx \frac{\mathcal{R}_p(\omega) k_p(\omega)}{k_{\parallel} - k_p(\omega)},$$

where $k_p(\omega)$ corresponds to the dispersion relation of the plasmons supported by the graphene sheet and $\mathcal{R}_p(\omega)$ is a dimensionless residue. Disregarding plasmonic losses (i.e, we take the imaginary part of k_p to be infinitesimal), we obtain

$$\text{Im}\{r_p(k_{\parallel}, \omega)\} \approx -i\pi \mathcal{R}_p(\omega) k_p(\omega) \delta[k_{\parallel} - k_p(\omega)]. \quad (\text{G3})$$

Plugging Eqs. (G2) and (G3) into Eq. (G1), we find

$$\begin{aligned} \Gamma_{\text{EELS}}^{(2)}(\mathbf{k}_{\parallel}, \omega) = & \frac{-2e^4}{\hbar^2 \pi^2 v^4} \int d\omega' \int k'_{\parallel} dk'_{\parallel} \int d\varphi \frac{|\mathbf{k}_{\parallel} - \mathbf{k}'_{\parallel}| \mathcal{R}_p(\omega - \omega') k_p(\omega - \omega')}{\left(|\mathbf{k}_{\parallel} - \mathbf{k}'_{\parallel}|^2 + (\omega - \omega')^2/v^2\right)^2} \frac{k'_{\parallel} \mathcal{R}_p(\omega') k_p(\omega')}{\left(k_{\parallel}^{\prime 2} + \omega'^2/v^2\right)^2} \\ & \times [n_{T_e}(\omega - \omega') + 1] [n_{T_e}(\omega) + 1] \delta[|\mathbf{k}_{\parallel} - \mathbf{k}'_{\parallel}| - k_p(\omega - \omega')] \delta[k'_{\parallel} - k_p(\omega')]. \end{aligned} \quad (\text{G4})$$

The last delta function in the second line of Eq. (G4) readily simplifies the k'_{\parallel} integral, effectively allowing us to set $k'_{\parallel} = k_p(\omega)$. In addition, noticing that $|\mathbf{k}_{\parallel} - \mathbf{k}'_{\parallel}| = \sqrt{k_{\parallel}^2 + k_p^2(\omega') - 2k_{\parallel} k_p(\omega') \cos(\varphi)}$ and making the change of variables $u = \cos(\varphi)$, we can rewrite the remaining delta function as

$$\delta[|\mathbf{k}_{\parallel} - \mathbf{k}'_{\parallel}| - k_p(\omega - \omega')] = \frac{k_p(\omega - \omega')}{k_{\parallel} k_p(\omega')} \delta(u - u_0),$$

with $u_0 = [k_{\parallel}^2 + k_p^2(\omega') - k_p^2(\omega - \omega')]/[2k_{\parallel} k_p(\omega')]$. After some straightforward algebra, we find that the two-plasmon loss probability reduces to

$$\Gamma_{\text{EELS}}^{(2)}(\mathbf{k}_{\parallel}, \omega) = \frac{4e^4}{\pi^2 \hbar^4 v^4} \int \frac{d\omega' \Pi(\omega - \omega') \Pi(\omega')}{\sqrt{4k_{\parallel}^2 k_p^2(\omega') - (k_{\parallel}^2 + k_p^2(\omega') - k_p^2(\omega - \omega'))^2}} \Theta \left[1 - \left| \frac{k_{\parallel}^2 + k_p^2(\omega') - k_p^2(\omega - \omega')}{2k_{\parallel} k_p(\omega')} \right| \right],$$

where

$$\Pi(\omega) = \frac{k_p(\omega)^3 \mathcal{R}_p(\omega)^3}{k_p(\omega)^2 + \omega^2/v^2} [n_{T_e}(\omega) + 1],$$

with the Heaviside function Θ originating in the integral over u , which is zero unless $|u_0| \leq 1$. We use this expression to obtain supplementary Figure 8, as it only involves a one-dimensional integral, so it is fast to compute.

VIII. ACKNOWLEDGMENTS

Spanish MINECO (MAT2017-88492-R and SEV2015-

This work has been supported in part by the European Research Council (Advanced Grant 789104-eNANO), the

TABLE I: Fitting parameters of the first six ribbon eigenvalues $1/\eta_{j,q} = \sum_m a_m q^m$ as a function of q . Parameters with an absolute value smaller than 10^{-4} are omitted.

j	a_{-4}	a_{-3}	a_{-2}	a_{-1}	a_0	a_1	a_2	a_3	a_4
1	1.14×10^{-4}	-1.5×10^{-2}	3.82×10^{-1}	-2.09	4.63	-6.13	7.71×10^{-2}	-2.66×10^{-3}	—
2	1.46×10^{-2}	-1.55	9.19	-1.82×10^1	3.72×10^{-1}	-4.65	-5.96×10^{-2}	2.45×10^{-3}	—
3	1.25×10^{-2}	-1.32	7.39	-1.29×10^1	-2.63×10^1	-1.81	-3.16×10^{-1}	1.01×10^{-2}	-1.21×10^{-4}
4	3.18×10^{-3}	-3.36×10^{-1}	1.82	-2.95	-5.27×10^1	-1.18×10^{-1}	-3.46×10^{-1}	9.48×10^{-3}	-1.02×10^{-4}
5	—	-8.43×10^{-3}	-9.83×10^{-3}	2.41×10^{-1}	-7.45×10^1	3.61×10^{-1}	-3.05×10^{-1}	7.24×10^{-3}	—
6	-1.14×10^{-3}	1.21×10^{-1}	-7.16×10^{-1}	1.4	-9.49×10^1	4.37×10^{-1}	-2.55×10^{-1}	5.14×10^{-3}	—

TABLE II: Ribbon eigenvectors u_j and v_j for $q = 0$. For each mode $j = 0$ to 10, the first 25 elements $v_{0,n}$ and $u_{j>0,n}$ of the corresponding eigenvector are presented. We omit elements $u_{0,n}$ and $v_{j>0,n} \approx 0$, which take negligible values. Vector elements smaller than 10^{-4} are also omitted.

n	$v_{0,n}$	$u_{1,n}$	$u_{2,n}$	$u_{3,n}$	$u_{4,n}$	$u_{5,n}$	$u_{6,n}$	$u_{7,n}$	$u_{8,n}$	$u_{9,n}$	$u_{10,n}$
1	-1.2732	-1.2004	—	0.3040	—	-0.1739	—	0.1217	—	0.0936	—
2	—	—	-1.2517	—	-0.5189	—	-0.3226	—	-0.2331	—	0.1821
3	-0.4237	0.1050	—	1.1736	—	-0.6517	—	0.4413	—	0.3311	—
4	—	—	0.3052	—	-1.0124	—	-0.7145	—	-0.5280	—	0.4132
5	-0.2535	0.0021	—	-0.4989	—	-0.7965	—	0.7073	—	0.5741	—
6	—	—	-0.0149	—	0.6716	—	-0.5425	—	-0.6365	—	0.5763
7	-0.1802	0.0010	—	0.0616	—	0.8005	—	0.2769	—	0.5133	—
8	—	—	0.0027	—	-0.1389	—	0.8758	—	-0.0184	—	0.3510
9	-0.1393	0.0004	—	-0.0072	—	-0.2396	—	-0.8897	—	-0.2104	—
10	—	—	0.0008	—	0.0193	—	-0.3559	—	0.8415	—	-0.3945
11	-0.1131	0.0002	—	-0.0009	—	0.0430	—	0.4752	—	-0.7361	—
12	—	—	0.0004	—	—	—	0.0820	—	-0.5860	—	-0.5826
13	-0.0948	—	—	-0.0006	—	-0.0032	—	-0.1372	—	0.6752	—
14	—	—	0.0002	—	0.0007	—	-0.0103	—	0.2084	—	0.7328
15	-0.0813	—	—	-0.0003	—	0.0010	—	0.0235	—	-0.2919	—
16	—	—	0.0001	—	0.0004	—	0.0019	—	-0.0453	—	-0.3828
17	-0.0708	—	—	-0.0002	—	0.0004	—	-0.0039	—	0.0774	—
18	—	—	—	—	0.0003	—	0.0004	—	0.0081	—	0.1212
19	-0.0624	—	—	-0.0001	—	0.0003	—	-0.0002	—	-0.0157	—
20	—	—	—	—	0.0002	—	0.0003	—	-0.0004	—	-0.0283
21	-0.0555	—	—	—	—	0.0002	—	-0.0003	—	0.0017	—
22	—	—	—	—	0.0001	—	0.0002	—	0.0004	—	0.0043
23	-0.0497	—	—	—	—	0.0001	—	-0.0002	—	-0.0006	—
24	—	—	—	—	—	—	0.0002	—	0.0002	—	-0.0010
25	-0.0448	—	—	—	—	—	—	-0.0002	—	-0.0002	—
26	—	—	—	—	—	—	0.0001	—	0.0002	—	-0.0002
27	-0.0405	—	—	—	—	—	—	-0.0001	—	-0.0002	—

0522), the European Commission (Graphene Flagship 696656), the Catalan CERCA Program, and Fundació Privada Cellex. F.C. acknowledges support from the ERC consolidator grant ISCQuM. E.J.C.D. acknowledges

financial support from “la Caixa” (INPhINIT Fellowship Grant 1000110434, LCF/BQ/DI17/11620057) and the EU (Marie Skłodowska-Curie Grant 713673).

-
- [1] G. Baffou and R. Quidant, *Laser Photon. Rev.* **7**, 171 (2012).
 - [2] G. X. Ni, L. Wang, M. D. Goldflam, M. Wagner, Z. Fei, A. S. McLeod, M. K. Liu, F. Keilmann, B. Özyilmaz, A. H. C. Neto, et al., *Nat. Photon.* **10**, 244 (2016).
 - [3] E. J. C. Dias, R. Yu, and F. J. García de Abajo, *Light Sci. Appl.* **9**, 87 (2020).
 - [4] P. C. Debnath, S. Uddin, and Y.-W. Song, *ACS Photonics* **5**, 445 (2018).
 - [5] J. D. Cox and F. J. García de Abajo, *Acc. Chem. Res.* **52**, 2536 (2019).
 - [6] W. Li, B. Chen, C. Meng, W. Fang, Y. Xiao, X. Li, Z. Hu, Y. Xu, L. Tong, H. Wang, et al., *Nano Lett.* **14**, 955 (2014).
 - [7] S. AbdollahRamezani, K. Arik, S. Farajollahi, A. Khavasi, and Z. Kavehvasht, *Opt. Lett.* **40**, 5383 (2015).
 - [8] R. Yu, Q. Guo, F. Xia, and F. J. García de Abajo, *Phys. Rev. Lett.* **121**, 057404 (2018).
 - [9] Y. D. Kim, Y. Gao, R.-J. Shiue, L. Wang, O. B. Aslan, M.-H. Bae, H. Kim, D. Seo, H.-J. Choi, S. H. Kim, et al., *Nano Lett.* **18**, 934 (2018).
 - [10] Q. Guo, R. Yu, C. Li, S. Yuan, B. Deng, F. J. García de Abajo, and F. Xia, *Nat. Mater.* **17**, 986 (2018).

- [11] K. P. H. Lui and F. A. Hegmann, *Appl. Phys. Lett.* **78**, 3478 (2001).
- [12] P. A. George, J. Strait, J. Dawlaty, S. Shivaraman, M. Chandrashekhara, F. Rana, and M. G. Spencer, *Nano Lett.* **8**, 4248 (2008).
- [13] S. Wall, D. Wegkamp, L. Foglia, K. Appavoo, J. Nag, R. F. Haglund, J. Stähler, and M. Wolf, *Nat. Commun.* **3**, 1 (2012).
- [14] F. J. García de Abajo, *Rev. Mod. Phys.* **82**, 209 (2010).
- [15] M. Kociak and O. Stéphan, *Chem. Soc. Rev.* **43**, 3865 (2014).
- [16] A. Polman, M. Kociak, and F. J. García de Abajo, *Nat. Mater.* **18**, 1158 (2019).
- [17] P. E. Batson, N. Dellby, and O. L. Krivanek, *Nature* **418**, 617 (2002).
- [18] O. L. Krivanek, T. C. Lovejoy, N. Dellby, T. Aoki, R. W. Carpenter, P. Rez, E. Soignard, J. Zhu, P. E. Batson, M. J. Lagos, et al., *Nature* **514**, 209 (2014).
- [19] M. J. Lagos, A. Trügler, U. Hohenester, and P. E. Batson, *Nature* **543**, 529 (2017).
- [20] F. S. Hage, R. J. Nicholls, J. R. Yates, D. G. McCulloch, T. C. Lovejoy, N. Dellby, O. L. Krivanek, K. Refson, and Q. M. Ramasse, *Sci. Adv.* **4**, eaar7495 (2018).
- [21] F. S. Hage, D. M. Kepaptsoglou, Q. M. Ramasse, and L. J. Allen, *Phys. Rev. Lett.* **122**, 016103 (2019).
- [22] J. A. Hachtel, J. Huang, I. Popovs, S. Jansone-Popova, J. K. Keum, J. Jakowski, T. C. Lovejoy, N. Dellby, O. L. Krivanek, and J. C. Idrobo, *Science* **363**, 525 (2019).
- [23] H. Boersch, J. Geiger, A. Imbusch, and N. Niedrig, *Phys. Lett.* **22**, 146 (1966).
- [24] R. B. Pettit, J. Silcox, and R. Vincent, *Phys. Rev. B* **11**, 3116 (1975).
- [25] C. H. Chen and J. Silcox, *Phys. Rev. Lett.* **35**, 390 (1975).
- [26] C. H. Chen and J. Silcox, *Solid State Commun.* **17**, 273 (1975).
- [27] M. Rocca, *Surf. Sci. Rep.* **22**, 1 (1995).
- [28] T. Nagao, T. Hildebrandt, M. Henzler, and S. Hasegawa, *Phys. Rev. Lett.* **86**, 5747 (2001).
- [29] M. S. Grinolds, V. A. Lobastov, J. Weissenrieder, and A. H. Zewail, *Proc. Natl. Acad. Sci.* **103**, 18427 (2006).
- [30] B. Barwick, H. S. Park, O. H. Kwon, J. S. Baskin, and A. H. Zewail, *Science* **322**, 1227 (2008).
- [31] B. Barwick, D. J. Flannigan, and A. H. Zewail, *Nature* **462**, 902 (2009).
- [32] A. Howie, *Inst. Phys. Conf. Ser.* **161**, 311 (1999).
- [33] F. J. García de Abajo and M. Kociak, *New J. Phys.* **10**, 073035 (2008).
- [34] A. Howie, *Microsc. Microanal.* **15**, 314 (2009).
- [35] E. Pomarico, I. Madan, G. Berruto, G. M. Vanacore, K. Wang, I. Kaminer, F. J. García de Abajo, and F. Carbone, *ACS Photonics* **5**, 759 (2018).
- [36] F. J. García de Abajo, A. Asenjo Garcia, and M. Kociak, *Nano Lett.* **10**, 1859 (2010).
- [37] S. T. Park, M. Lin, and A. H. Zewail, *New J. Phys.* **12**, 123028 (2010).
- [38] L. Piazza, T. T. A. Lummen, E. Quiñonez, Y. Murooka, B. Reed, B. Barwick, and F. Carbone, *Nat. Commun.* **6**, 6407 (2015).
- [39] A. Feist, K. E. Echternkamp, J. Schauss, S. V. Yalunin, S. Schäfer, and C. Ropers, *Nature* **521**, 200 (2015).
- [40] T. T. A. Lummen, R. J. Lamb, G. Berruto, T. LaGrange, L. D. Negro, F. J. García de Abajo, D. McGrouther, B. Barwick, and F. Carbone, *Nat. Commun.* **7**, 13156 (2016).
- [41] K. E. Echternkamp, A. Feist, S. Schäfer, and C. Ropers, *Nat. Phys.* **12**, 1000 (2016).
- [42] K. E. Priebe, C. Rathje, S. V. Yalunin, T. Hohage, A. Feist, S. Schäfer, and C. Ropers, *Nat. Photon.* **11**, 793 (2017).
- [43] G. M. Vanacore, I. Madan, G. Berruto, K. Wang, E. Pomarico, R. J. Lamb, D. McGrouther, I. Kaminer, B. Barwick, F. J. García de Abajo, et al., *Nat. Commun.* **9**, 2694 (2018).
- [44] G. M. Vanacore, G. Berruto, I. Madan, E. Pomarico, P. Biagioni, R. J. Lamb, D. McGrouther, O. Reinhardt, I. Kaminer, B. Barwick, et al., *Nat. Mater.* **18**, 573 (2019).
- [45] O. Kfir, H. Lourenço-Martins, G. Storeck, M. Sivilis, T. R. Harvey, T. J. Kippenberg, A. Feist, and C. Ropers, *Nature* **582**, 46 (2020).
- [46] K. Wang, R. Dahan, M. Shentcis, Y. Kauffmann, A. B. Hayun, O. Reinhardt, S. Tsesses, and I. Kaminer, *Nature* **582**, 50 (2020).
- [47] S. Vogelgesang, G. Storeck, J. G. Horstmann, T. Diekmann, M. Sivilis, S. Schramm, K. Rossnagel, S. Schäfer, and C. Ropers, *NPhy* **14**, 184 (2018).
- [48] A. Konečná, V. Di Giulio, V. Mkhitarian, C. Ropers, and F. J. García de Abajo, *ACS Photonics* **7**, 1290 (2019).
- [49] M. Jablan, H. Buljan, and M. Soljačić, *Phys. Rev. B* **80**, 245435 (2009).
- [50] Z. Fei, G. O. Andreev, W. Bao, L. M. Zhang, A. S. McLeod, C. Wang, M. K. Stewart, Z. Zhao, G. Dominguez, M. Thiemens, et al., *Nano Lett.* **11**, 4701 (2011).
- [51] F. H. L. Koppens, D. E. Chang, and F. J. García de Abajo, *Nano Lett.* **11**, 3370 (2011).
- [52] J. Chen, M. Badioli, P. Alonso-González, S. Thongrattanasiri, F. Huth, J. Osmond, M. Spasenović, A. Centeno, A. Pesquera, P. Godignon, et al., *Nature* **487**, 77 (2012).
- [53] Z. Fei, A. S. Rodin, G. O. Andreev, W. Bao, A. S. McLeod, M. Wagner, L. M. Zhang, Z. Zhao, M. Thiemens, G. Dominguez, et al., *Nature* **487**, 82 (2012).
- [54] H. Yan, X. Li, B. Chandra, G. Tulevski, Y. Wu, M. Freitag, W. Zhu, P. Avouris, and F. Xia, *Nat. Nanotech.* **7**, 330 (2012).
- [55] H. Yan, Z. Li, X. Li, W. Zhu, P. Avouris, and F. Xia, *Nano Lett.* **12**, 3766 (2012).
- [56] V. W. Brar, M. S. Jang, M. Sherrott, J. J. Lopez, and H. A. Atwater, *Nano Lett.* **13**, 2541 (2013).
- [57] A. Woessner, M. B. Lundeberg, Y. Gao, A. Principi, P. Alonso-González, M. Carrega, K. Watanabe, T. Taniguchi, G. Vignale, M. Polini, et al., *Nat. Mater.* **14**, 421 (2015).
- [58] G. X. Ni, A. S. McLeod, Z. Sun, L. Wang, L. Xiong, K. W. Post, S. S. Sunku, B.-Y. Jiang, J. Hone, C. R. Dean, et al., *Nature* **557**, 530 (2018).
- [59] M. B. Lundeberg, Y. Gao, R. Asgari, C. Tan, B. V. Duppen, M. Autore, P. Alonso-González, A. Woessner, K. Watanabe, T. Taniguchi, et al., *Science* **357**, 187 (2017).
- [60] D. Alcaraz Iranzo, S. Nanot, E. J. C. Dias, I. Epstein, C. Peng, D. K. Efetov, M. B. Lundeberg, R. Parret, J. Osmond, J.-Y. Hong, et al., *Science* **360**, 291 (2018).

- [61] N. Kumar, J. Kumar, C. Gerstenkorn, R. Wang, H.-Y. Chiu, A. L. Smirl, and H. Zhao, *Phys. Rev. B* **87**, 121406(R) (2013).
- [62] B. Yao, Y. Liu, S.-W. Huang, C. Choi, Z. Xie, J. F. Flores, Y. Wu, M. Yu, D.-L. Kwong, Y. Huang, et al., *Nat. Photon.* **12**, 22 (2018).
- [63] D. Kundys, B. V. Duppen, O. P. Marshall, F. Rodriguez, I. Torre, A. Tomadin, M. Polini, and A. N. Grigorenko, *Nano Lett.* **18**, 282 (2018).
- [64] F. N. Xia, T. Mueller, Y. M. Lin, A. Valdes-Garcia, and P. Avouris, *Nat. Nanotech.* **4**, 839 (2009).
- [65] F. Koppens, T. Mueller, P. Avouris, A. Ferrari, M. Vitiello, and M. Polini, *Nat. Nanotech.* **9**, 780 (2014).
- [66] M. B. Lundeborg, Y. Gao, A. Woessner, C. Tan, P. Alonso-González, K. Watanabe, T. Taniguchi, J. Hone, R. Hillenbrand, and F. H. L. Koppens, *Nat. Mater.* **16**, 204 (2017).
- [67] S. Yuan, R. Yu, C. Ma, B. Deng, Q. Guo, X. Chen, C. Li, C. Chen, K. Watanabe, T. Taniguchi, et al., *ACS Photonics* **7**, 1206 (2020).
- [68] D. Rodrigo, O. Limaj, D. Janner, D. Etezadi, F. J. García de Abajo, V. Pruneri, and H. Altug, *Science* **349**, 165 (2015).
- [69] H. Hu, X. Yang, F. Zhai, D. Hu, R. Liu, K. Liu, Z. Sun, and Q. Dai, *Nat. Commun.* **7**, 12334 (2016).
- [70] H. Hu, X. Yang, X. Guo, K. Khaliji, R. Biswas, F. J. García de Abajo, T. Low, Z. Sun, and Q. Dai, *Nat. Commun.* **10**, 1131 (2019).
- [71] F. J. García de Abajo, *ACS Photonics* **1**, 135 (2014).
- [72] Y. Gao, R.-J. Shiue, X. Gan, L. Li, C. Peng, I. Meric, L. Wang, A. Szep, D. W. Jr., J. Hone, et al., *Nano Lett.* pp. 2001–2005 (2015).
- [73] O. Vafek, *Phys. Rev. Lett.* **97**, 266406 (2006).
- [74] M. M. Jadidi, J. C. König-Otto, S. Winnerl, A. B. Sushkov, H. D. Drew, T. E. Murphy, and M. Mitterdorff, *Nano Lett.* **16**, 2734 (2016).
- [75] J. C. Johannsen, S. Ulstrup, F. Cilento, A. Crepaldi, M. Zacchigna, C. Cacho, I. C. E. Turcu, E. Springate, F. Fromm, C. Roidel, et al., *Phys. Rev. Lett.* **111**, 027403 (2013).
- [76] I. Gierz, J. C. Petersen, M. Mitrano, C. Cacho, I. C. E. Turcu, E. Springate, A. Stöhr, A. Köhler, U. Starke, and A. Cavalleri, *Nat. Mater.* **12**, 1119 (2013).
- [77] R. R. Nair, P. Blake, A. N. Grigorenko, K. S. Novoselov, T. J. Booth, T. Stauber, N. M. R. Peres, and A. K. Geim, *Science* **320**, 1308 (2008).
- [78] J. M. Hamm, A. F. Page, J. Bravo-Abad, F. J. Garcia-Vidal, and O. Hess, *Phys. Rev. B* **93**, 041408 (2016).
- [79] H. Boersch, J. Geiger, and W. Stickel, *Phys. Rev. Lett.* **17**, 379 (1966).
- [80] M. J. Lagos and P. E. Batson, *Nano Lett.* **18**, 4556 (2018).
- [81] R. Yu, A. Manjavacas, and F. J. García de Abajo, *Nat. Commun.* **8**, 2 (2017).
- [82] F. J. García de Abajo, *ACS Nano* **7**, 11409 (2013).
- [83] J. Christensen, A. Manjavacas, S. Thongrattanasiri, F. H. L. Koppens, and F. J. García de Abajo, *ACS Nano* **6**, 431 (2012).
- [84] A. A. Lucas and M. Šunjić, *Progr. Surf. Sci.* **2**, 75 (1972).
- [85] A. A. Lucas and E. Kartheuser, *Phys. Rev. B* **1**, 3588 (1970).
- [86] B. Wunsch, T. Stauber, F. Sols, and F. Guinea, *New J. Phys.* **8**, 318 (2006).
- [87] E. H. Hwang and S. Das Sarma, *Phys. Rev. B* **75**, 205418 (2007).
- [88] P. F. Maldague, *Surf. Sci.* **73**, 296 (1978).
- [89] N. D. Mermin, *Phys. Rev. B* **1**, 2362 (1970).
- [90] S. I. Anisimov, B. L. Kapeliovich, and T. L. Perel'man, *J. Exp. Theor. Phys.* **41**, 375 (1974).
- [91] J. C. W. Song, M. Y. Reizer, and L. S. Levitov, *Phys. Rev. Lett.* **109**, 106602 (2012).
- [92] L. X. Benedict, S. G. Louie, and M. L. Cohen, *Solid State Commun.* **100**, 177 (1996).
- [93] O. V. Shapoval, R. Sauleau, and A. I. Nosich, *IEEE Trans. Antennas Propag.* **59**, 3339 (2011).
- [94] J. L. Tsalamengas, J. G. Fikioris, and B. T. Babili, *J. Appl. Phys.* **66**, 69 (1989).
- [95] A. Khavasi and B. Rejaei, *IEEE J. Quantum Electron.* **50**, 397 (2014).
- [96] R. Yu, J. D. Cox, J. R. M. Saavedra, and F. J. García de Abajo, *ACS Photonics* **4**, 3106 (2017).
- [97] P. A. D. Gonçalves, N. Stenger, J. D. Cox, N. A. Mortensen, and S. Xiao, *Adv. Opt. Mater.* **8**, 1901473 (2020).
- [98] J. P. Boyd, *Chebyshev and Fourier spectral methods* (Courier Corporation, New York, 2001).
- [99] F. W. J. Olver, D. W. Lozier, R. F. Boisvert, and C. W. Clark, *NIST Handbook of Mathematical Functions Hardback and CD-ROM* (Cambridge University Press, New York, 2010).
- [100] J. Wimp, *Math. Comput.* **16**, 446 (1962).
- [101] E. J. C. Dias and F. J. García de Abajo, *ACS Nano* **13**, 5184 (2019).

IX. SUPPLEMENTARY FIGURES

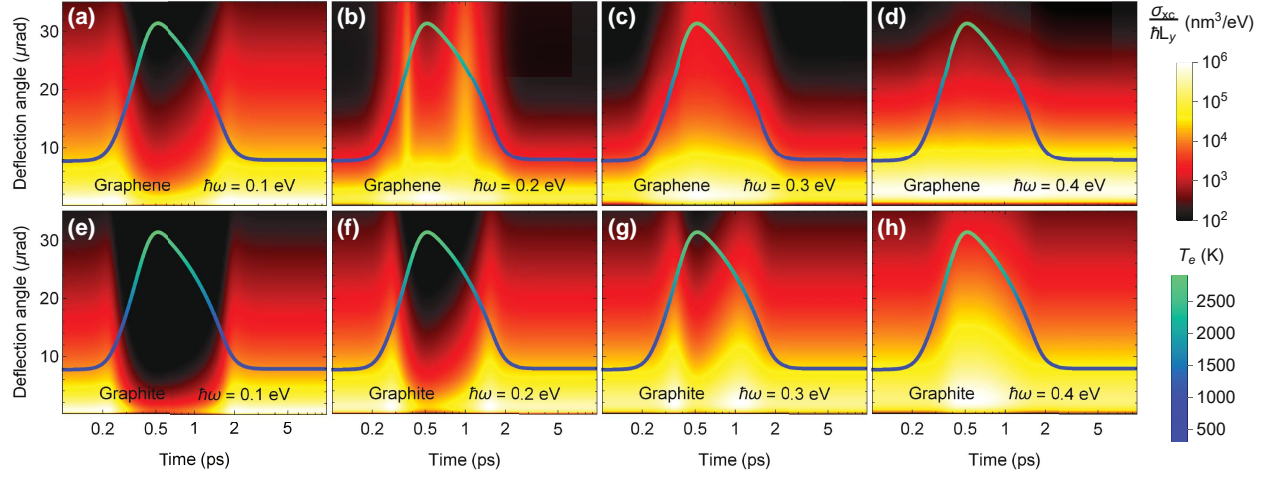


FIG. 5: Same as Figure 1c, but for (a-d) graphene (0.2 eV Fermi energy, 4 meV intrinsic damping) and (e-h) graphite (undoped, 10 monolayers) 100-nm-wide ribbons with different selected energy losses $\hbar\omega$ (see labels), illuminated by a Gaussian pump pulse of 166.5 fs FWHM delivering 100 GW/m^2 peak absorption power density, and probed with 100 keV electrons. The density plots show the inelastic cross section $\sigma_{xc}(\mathbf{k}_{\parallel}, \omega)$ resolved in lateral momentum $\hbar\mathbf{k}_{\parallel}$ and energy $\hbar\omega$ transfers.

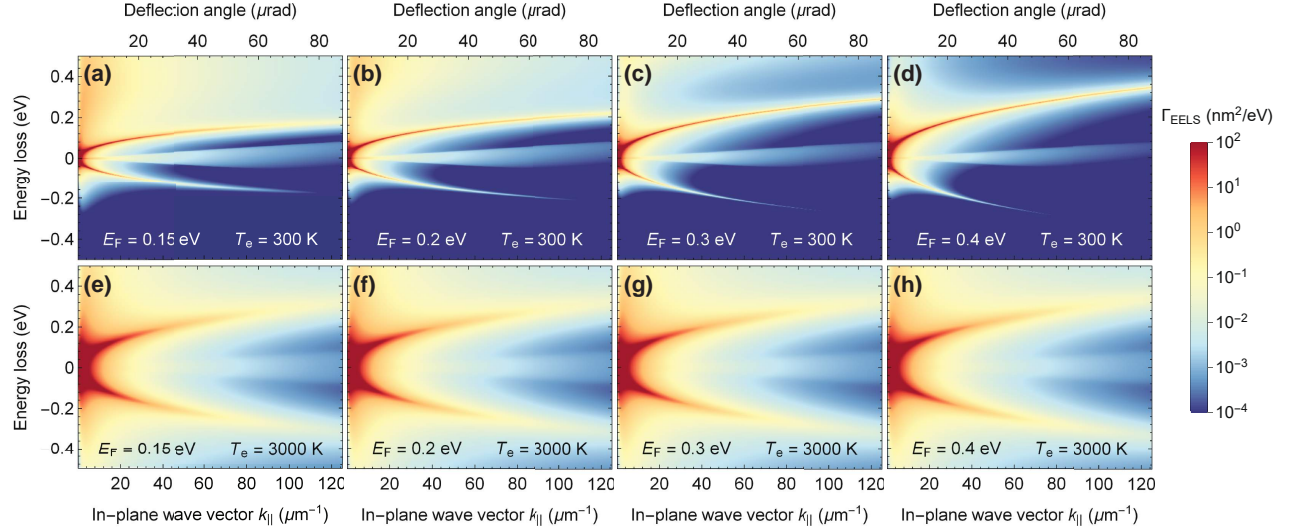


FIG. 6: Same as Figure 2c,d, but for different Fermi energies (see labels). We consider low and high temperatures in the upper and lower plots, respectively.

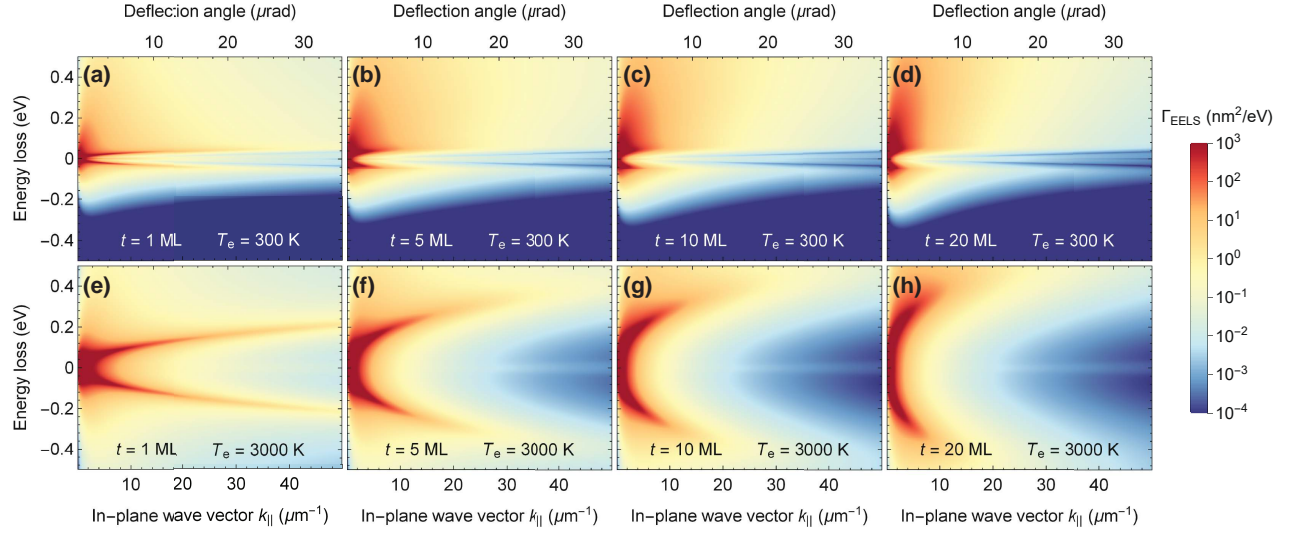


FIG. 7: Same as Figure 2c,d, but for undoped multilayer graphene films with different numbers of carbon monolayers (MLs, see labels). We consider low and high temperatures in the upper and lower plots, respectively.

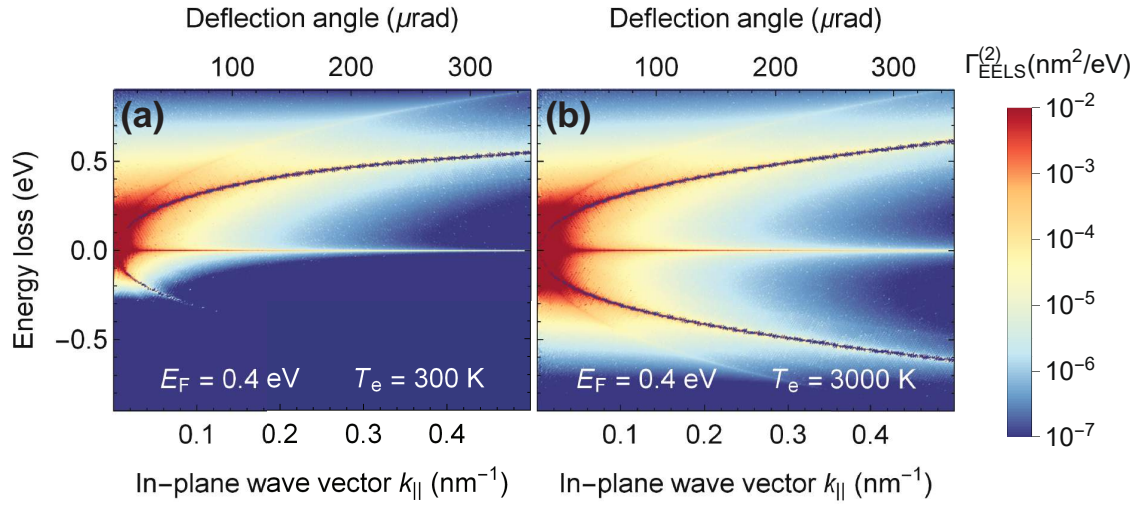


FIG. 8: Same as Figure 2c,d, but a Fermi energy $E_F = 0.4$ eV and including multiple scattering events (see Sec. G for details of the calculation). The first replica of the plasmon dispersion is clearly discernible. The dominant plasmon feature is now sharper than in Figure 2 because we are neglecting the intrinsic graphene damping. A faint plasmon replica indicates the two-plasmon excitation processes.

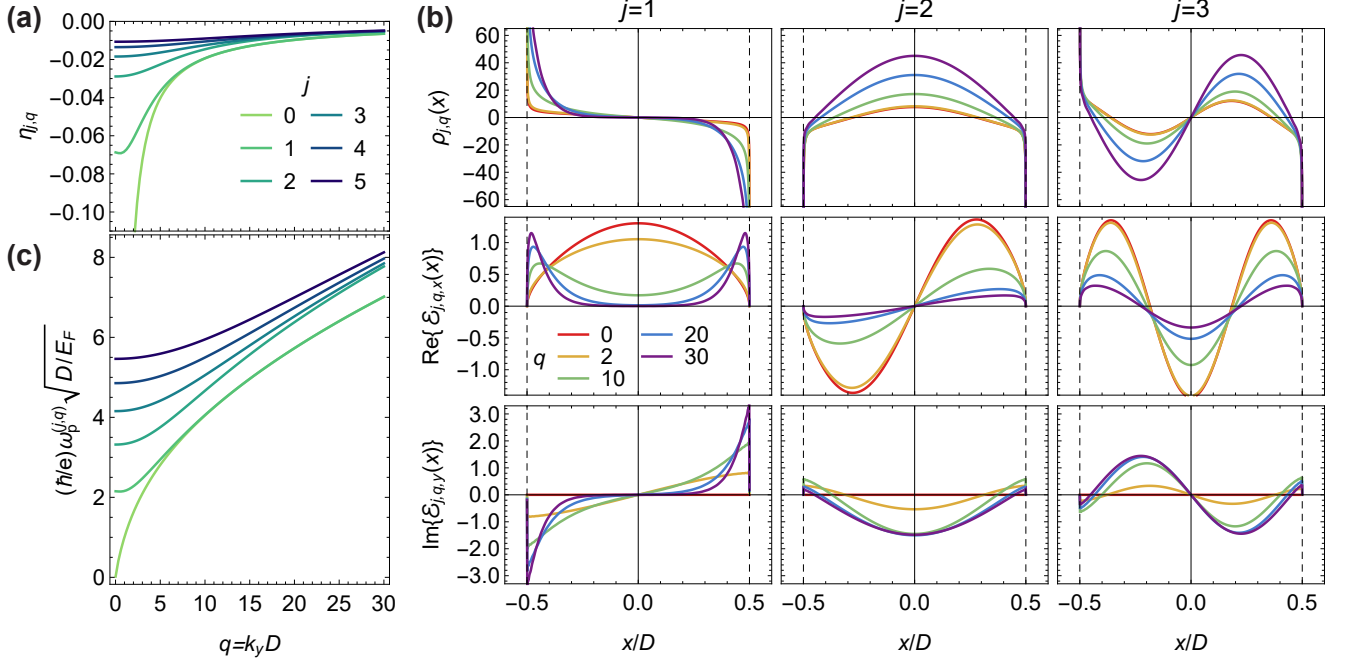


FIG. 9: Electrostatic eigenmodes of a ribbon. (a) Momentum dependence of the eigenvalues η_s (with $s = \{j, q\}$) for the six lowest-order modes. (b) The corresponding charge distributions (top, $\rho_j(x)$) and electric fields (middle, $\mathcal{E}_{sx}(x)$; bottom, $\mathcal{E}_{sy}(x)$) of modes $j = 1-3$ (see top labels) for different values of the normalized parallel wave vector $q = k_y D$ as a function of transverse ribbon position coordinate x normalized to the ribbon width D . (c) Dispersion relation of the first six plasmonic modes of a graphene ribbon in the Drude model, as calculated from Eq. (F6).

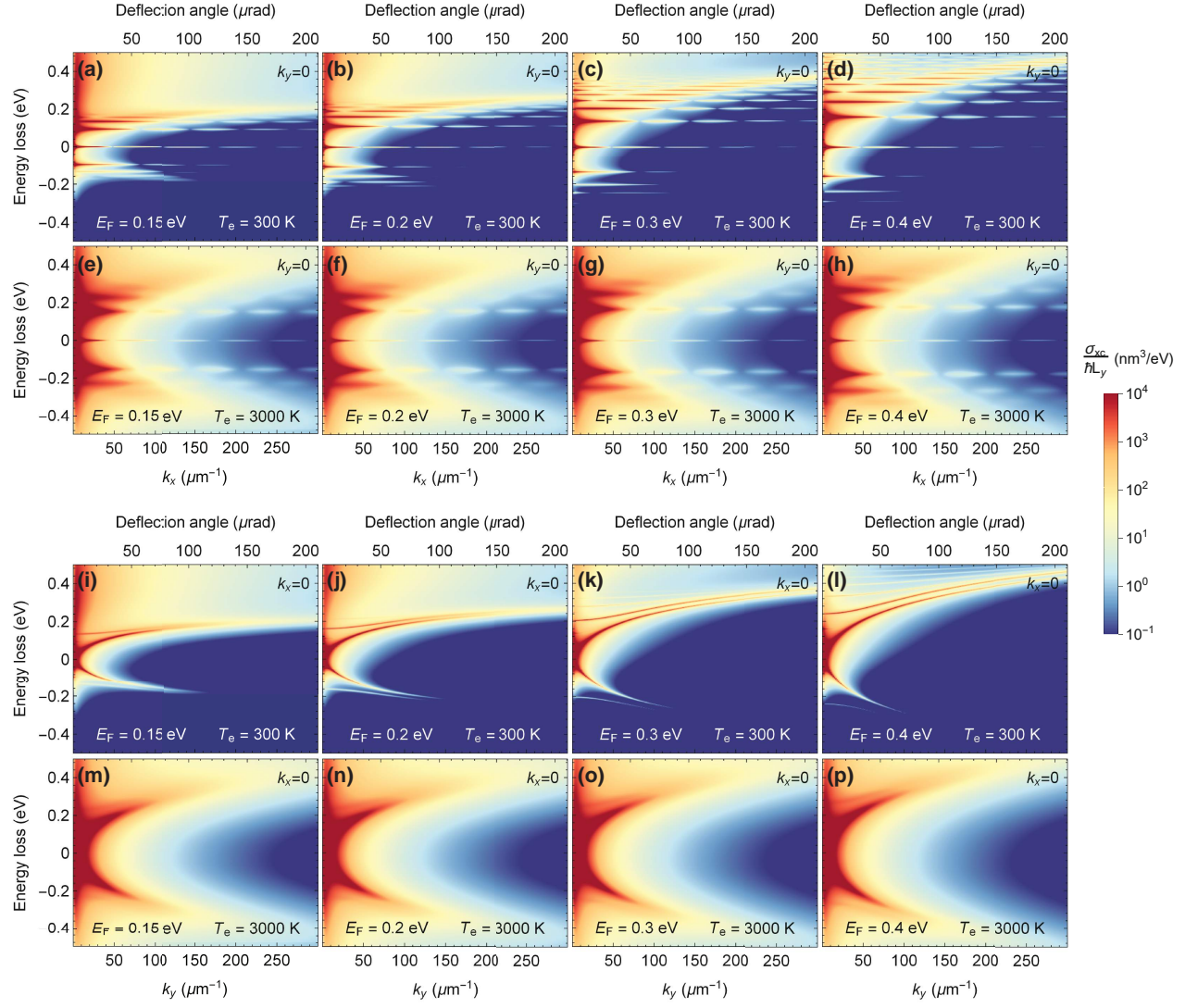


FIG. 10: Same as Figure 3b-e, but for graphene ribbons with different Fermi energies E_F (see labels). The ribbon width is 100 nm in all cases.

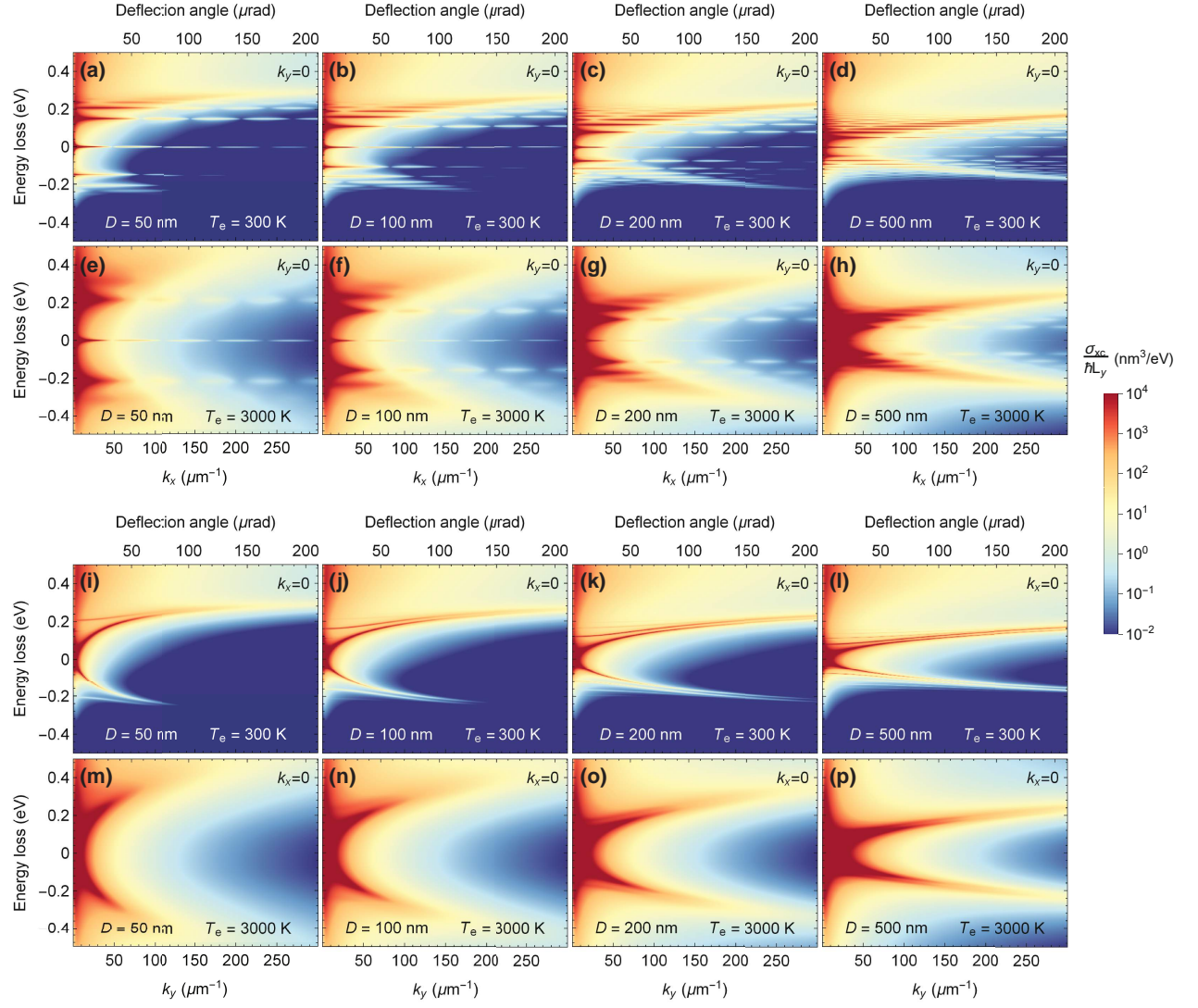


FIG. 11: Same as Figure 3b-e, but for graphene ribbons with widths D (see labels). The Fermi energy is $E_F = 0.4$ eV in all cases.

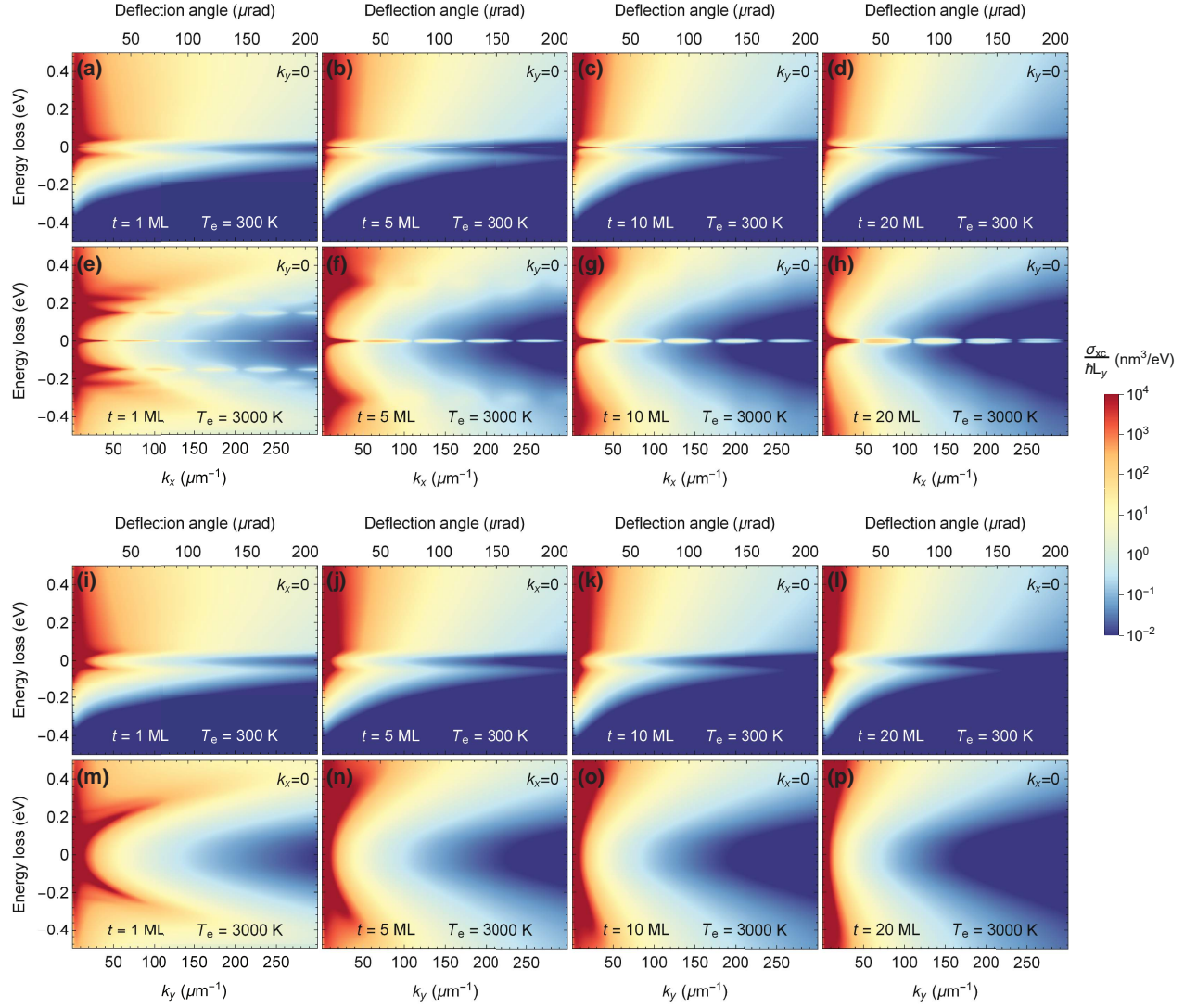


FIG. 12: Same as Figure 3g-j, but for undoped multilayer graphene ribbons with different numbers of carbon monolayers (MLs, see labels). The ribbon width is 100 nm in all cases.

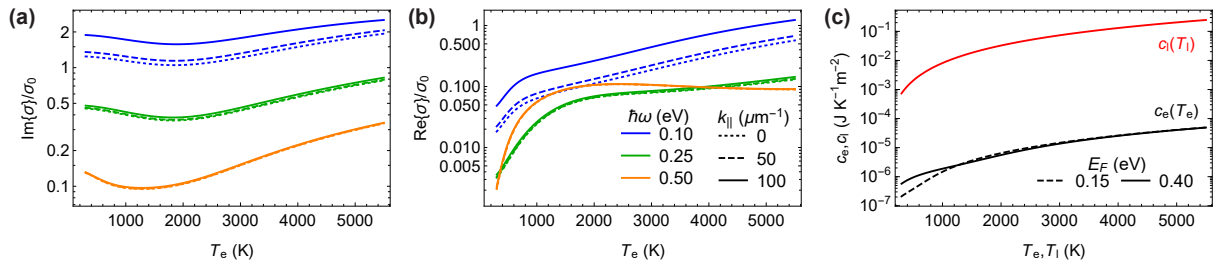


FIG. 13: Temperature-dependent properties of extended graphene. (a) Imaginary and (b) real parts of the conductivity as a function of electronic temperature T_e for different values of the parallel wave vector k_{\parallel} and frequency ω with a Fermi energy $E_F = 0.4$ eV. The conductivity is normalized to $\sigma_0 = e^2/h$. (c) Electronic (black) and lattice (red) heat capacities as a function of electronic and lattice temperatures, respectively, for two different values of the Fermi energy (see labels).